

Numerical Evaluation of a Novel Slot-Drill Enhanced Oil Recovery Technology for Tight Rocks

Hassan Amer¹ and Olufemi Olorode^{1*}

¹Louisiana State University

Summary

Enhanced oil recovery (EOR) is essential in shale/tight formations because primary recovery typically produces less than 10% of the original hydrocarbon in place. This work presents a novel “slot-drill” EOR (SDEOR) technology, which involves injecting gas through a horizontal fracture that is cut into the formation near the top of the reservoir (using a tensioned abrasive cable mounted to the drillstring) and producing oil from a second slot-drilled horizontal fracture near the bottom of the reservoir.

A robust 3D projection-based embedded discrete fracture model (pEDFM; EDFM) is used to model the natural fractures in these slot-drilled unconventional oil reservoirs accurately and efficiently. Connectivity and uncertainty analyses are performed to determine the percolation threshold, where natural fractures influence hydrocarbon production appreciably. The results of this work indicate that the proposed technology can yield over a threefold increase in oil recovery relative to the cyclic gas EOR (CGEOR) method. This simulated recovery is high regardless of the presence of natural fractures or the type of gas/solvent injected (such as CH₄, N₂, CO₂, and flue gas). The simulation results also indicate that the continuous gas injection, higher relative oil permeability, and the role of gravity-drainage are the main reasons why the oil recovery from the SDEOR is three times that from the CGEOR method.

In conclusion, this is the first presentation and numerical simulation study of applying pairs of parallel slot-drilled fractures to enhance the recovery from challenging unconventional reservoirs (such as the Bakken shale) that have not been successfully enhanced using the CGEOR method. The dramatic increase in recovery from SDEOR, coupled with its applicability regardless of the stress state or formation brittleness, could change how unconventional reservoirs are completed and produced in the future.

Introduction

The combination of horizontal drilling and multistage hydraulic fracturing has resulted in the commercial development of tight or shale oil resources. Over the last 15 years, the advancements in drilling and completion technologies have enabled us to drill wells with longer lateral lengths and to create several fracture clusters at several stages in the well. However, shale-oil wells are reported to decline by 75 to 90% within the first 3 years of production, producing only 5 to 9% of the amount of oil initially in the reservoir (Kuuskraa et al. 2020; Hakso and Zoback 2019; Hughes 2018). This has stimulated considerable interest in the study of EOR in tight rocks and resulted in several related publications over the last decade (Yu et al. 2014; Sun et al. 2016; Zhu et al. 2017). The general idea in virtually all of these previous shale EOR studies involves injecting fluids (mostly CO₂ or hydrocarbon gas) through multistage hydraulic fractures. The injection can either be continuous (through an injection well) or cyclic (in huff 'n' puff mode) as in conventional EOR. Of these two, the CGEOR has proved to be the most appropriate, based on field and pilot studies in the Eagle Ford shale play (Grinestaff et al. 2020; Pankaj et al. 2018; Kerr et al. 2020).

Considering the significant costs of injecting fluids into shale-oil reservoirs, petroleum engineers typically perform numerical simulation to identify the optimum EOR mechanism, operating constraints, and injection mode, among others. However, these numerical studies are complicated by the common occurrence of natural fractures in unconventional oil and gas reservoirs. As mentioned in Apiwathanasorn and Ehlig-Economides (2012), different authors have conflicting views on the significance of the contribution of natural fractures in unconventional oil and gas reservoirs. This, coupled with the computational challenge of accounting for each of the natural fractures in a reservoir, has contributed to the proliferation of several shale EOR publications that use effective matrix/fracture models [such as dual porosity, dual permeability, and continuum models, as in Warren and Root (1963) and Pruess and Narasimhan (1982)], or simply neglect the presence of natural fractures. Unlike the effective medium models, discrete models [such as discrete fracture models by Kim and Deo (2000) and Karimi-Fard and Firoozabadi (2001); EDFM by Li and Lee (2008); pEDFM by Tene et al. (2017); etc.] are able to account for each individual fracture in a naturally fractured reservoir.

Regardless of the fracture model used, the increase in recovery from CGEOR methods appear to be much less than the proposed shale EOR method. For instance, Moridis and Reagan (2020) used a single-porosity effective matrix/fracture model and showed that the injection of methane gas using the CGEOR method did not result in an appreciable increase in oil recovery (relative to primary production). Various authors (Dahaghi 2010; Eshkalak et al. 2014; Kim et al. 2015) have also used the dual continuum models to evaluate CO₂ continuous and cyclic injection shale-oil reservoirs. Although these methods are computationally faster, they are unable to account for the heterogeneity in the individual fracture sizes, orientation, distribution, and so on. So, we focus on the numerical simulation studies of the conventional shale EOR methods using EDFM. **Table 1** [modified from Du and Nojabaei (2019)] summarizes some of these EDFM simulation results and provides the corresponding references. These tabulated results as well as the other numerical and experimental studies summarized in Tables 1 and 2 of Du and Nojabaei (2019) indicate a wide range in the increased oil recovery factor (RF) reported by various authors. In line with previous shale EOR studies, we quantify the increase in oil recovery using the improved oil recovery (IOR) ratio, which is the ratio of the expected ultimate recovery (EUR) from EOR to the EUR from primary recovery.

*Corresponding author; email: olorode@lsu.edu

Copyright © 2022 Society of Petroleum Engineers

Original SPE manuscript received for review 29 June 2021. Revised manuscript received for review 12 January 2022. Paper (SPE 209597) peer approved 14 January 2022. Supplementary materials are available in support of this paper and have been published online under Supplementary Data at <https://doi.org/10.2118/209597-PA>. SPE is not responsible for the content or functionality of supplementary materials supplied by the authors.

Formation	k_m (μd)	Injected Gas	Injection Mode	Production Period (years)	Increased Oil RF (%)	Reference
Middle Bakken	1	CO ₂	Huff 'n' puff	18	+2.56	Zuloaga et al. (2017)
Middle Bakken	1	CO ₂	Continuous flooding	18	-1.79	Zuloaga et al. (2017)
Middle Bakken	20	CO ₂	Huff 'n' puff	20	+5.9 (3 cycles)	Sun et al. (2019)
Eagle Ford	0.9	CO ₂	Huff 'n' puff	20	+8 (D_{CO_2} = 0.01 cm ² /s)	Yu et al. (2019)
Eagle Ford	0.334	Field gas	Huff 'n' puff	5	+8.75 (single well and 10 cycles)	Ganjdanesh et al. (2019)

Table 1—A summary of EDFM simulation results for EOR gas injection into different fractured shale oil formations (Du and Nojabaei 2019).

Considering that EDFM is unable to account for low-conductivity fractures accurately (Tene et al. 2017), the EDFM studies in **Table 1** implicitly assume that all the natural fractures are conductive, which is unlikely in reality. This is because the orientation of each fracture depends on the prevailing stress state when it was created (Shafiei et al. 2018), after which fine-grained/cementing materials could accumulate in these fractures and make them sealing in the prevailing stress state today. In this work, we use the pEDFM to evaluate the performance of the proposed technology in naturally fractured reservoirs with any arbitrary fracture conductivity.

The application of CGEOR in field and pilot studies has yielded mixed results. Several authors agree that CGEOR has been successful in the Eagle Ford shale, with IOR ratios ranging from 1.3 to 1.7 (Hoffman 2018; Grinestaff et al. 2020). However, the application of CGEOR has been unsuccessful in the Bakken shale play (Hoffman and John 2016). Although Rassenfoss (2017) attributed the lack of an incremental oil recovery to the lower matrix permeability of the Bakken, Hoffman and John (2016) concluded (from his analysis of several EOR field/pilot tests) that early gas breakthrough (or connectivity of the fracture networks with those from offset wells) rather than poor injectivity was the cause of the negligible increment in recovery. Although field and pilot studies of the CGEOR in the Eagle Ford play indicate an IOR ratio of up to 1.7 if hydrocarbon gases are injected at high rates, Jacobs (2019) pointed out that the success of CGEOR in a shale play depends on its fluid and fracture network properties. The SDEOR technology presented in this work can yield IOR ratios of up to 4.17 within 8 years of production, even with fluid, matrix, and fracture properties that are representative of the Bakken shale. Although SDEOR outperforms CGEOR for all the cases simulated with representative Bakken and Eagle Ford shale parameters, it is worth noting that this technology is yet to be validated by experiments and in the field, and it will not apply in thin shales because the pair of slot-drilled horizontal fractures will be too close to be commercially viable. So, the overarching goal in this paper is to propose a different EOR approach that could be applicable in various tight rocks.

This paper is structured to begin with an introduction of the proposed slot-drill EOR technology and why it could be feasible and game-changing in shale plays in any prevailing stress regime, with or without natural fractures, and which may or may not be brittle. We then discuss how natural fractures are modeled in this work, after which we analyze their connectivity to understand their role in primary and enhanced recovery from the proposed technology. We then perform short- and long-term studies of SDEOR in fractured shale oil reservoirs before performing a reasonable comparison of the oil production from SDEOR to that from CGEOR under similar conditions. Next, we evaluate the role of different recovery mechanisms on the EOR from SDEOR and conclude with a numerical study of the application of SDEOR to Eagle Ford and Bakken shale plays using different fracture conductivities and injectants. Finally, we present the simulation results for the performance of the SDEOR in extreme cases in the Supplementary Material provided with this paper.

Proposed Slot-Drill EOR Technology

The slot-drill (SD) technology is based on ideas involving using a chain cutter that is pulled through massive rock outcrops, as in Hurd (1980) and Farrar et al. (1991). The proposed application of this concept to cut fractures in the subsurface involves the use of one or more wells. Coleman and Hester (2010) proposed drilling two wellbores either from two different wellheads or side-tracked from one well. These wellbores are connected at the toe using hook and ring-like steel tools. A flexible and tensioned cutting cable (“wire saw”) is then passed through one of the wellbores’ ring-like structure and fished out from the other wellbore with the steel hook. The cable is then pulled back and forth from the wellhead to cut a slot-drilled fracture the rock mass between the two wellbores. Carter (2011) proposed the use of a single well to cut fractures in the horizontal direction, as shown in **Fig. 1** (from <https://cartertech.com/alternatives-to-hydraulic-fracturing>).

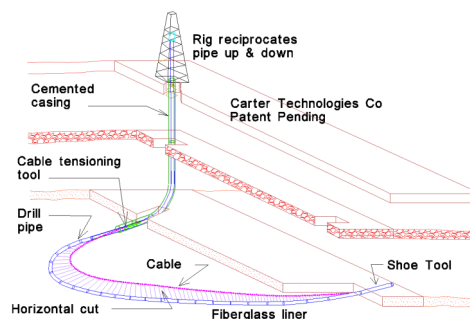


Fig. 1—This image illustrates how to create a horizontal fracture using the slot-drill completion technique. Image was culled from <https://cartertech.com/alternatives-to-hydraulic-fracturing> (Carter 2011).

In this paper, we introduce and numerically evaluate a novel EOR technique where gas is injected into horizontal fractures created close to the top of the reservoir, while oil is produced from parallel horizontal fractures created close to the bottom of the reservoir. To

create these horizontal fractures regardless of the prevailing stress states in the reservoir, this work suggests the use of the slot-drilling completion technique (Carter 2011), where the subsurface rock can be cut using tensioned abrasive cables attached to the drillpipe, as shown in Fig. 1. Under primary recovery, Odunowo et al. (2014) concluded that multistage hydraulic fractures (MSHF) outperformed the SD completion because of their larger fracture areas. Although two wells are typically recommended to create an SD completion (as shown in Fig. 1), only one of them is needed for primary production. Here, we propose the use of both wells to create two parallel horizontal fractures, as illustrated in Fig. 2. After the two fractures are created, one of the wells gets plugged at the bottom and is only allowed to inject fluids at the top, while the other is open to flow from the bottom fracture. Although this work focuses on the injection of gases at the top while oil is produced from the bottom, it can also be set up to inject water at the bottom while oil is produced from the top.

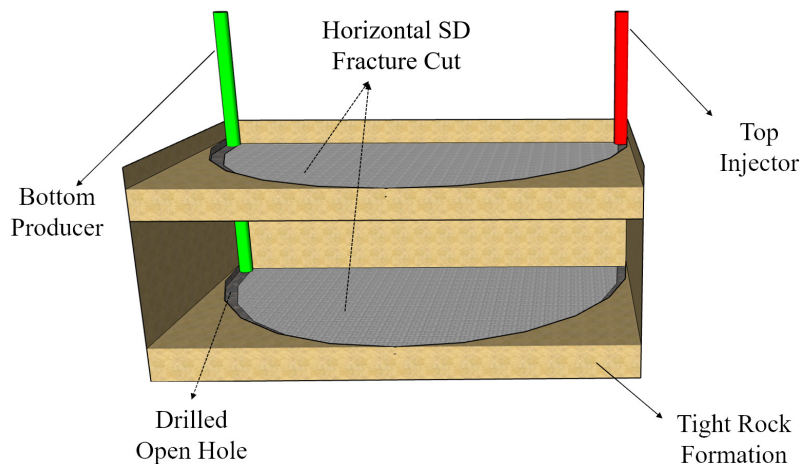


Fig. 2—This sketch illustrates the proposed SDEOR technology, where the gas/solvent is injected into the top injector (which is completed in the top fracture) and oil is produced from the bottom producer (which is completed in the bottom fracture).

Fig. 3 shows the mesh generated to model the simulation domain described in Fig. 2. The two slot-drilled fractures are meshed explicitly, as shown in yellow, and the size of the cells are increased geometrically away from fracture. This is to capture the expected transient behavior near the fracture surfaces. Considering that there is currently no technology available to find the location, size, orientation, and properties of all fractures in the subsurface, this work will also involve the simulation of several realizations of natural fracture networks (in addition to the slot-drilled fractures). This will enable the quantification of the effect of these uncertainties on the effectiveness of the proposed SDEOR method.

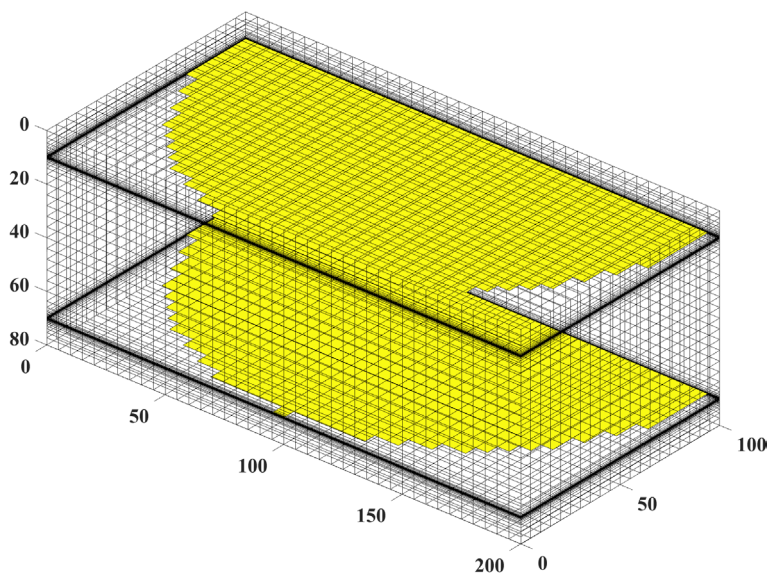


Fig. 3—This image shows the meshing of the simulation domain for the proposed SDEOR technology. The cell sizes are increased geometrically away from the two fracture surfaces (in yellow), located at 10 and 70 m from the top of the reservoir.

To evaluate the performance of the SDEOR technology in shale oil reservoirs with realistic fracture networks, we will perform compositional simulation studies using our open source “shale” module, which is distributed as part of the latest version of MATLAB Reservoir Simulation Toolbox (version 2020b). This module essentially implements the 3D pEDFM presented in Olorode et al. (2020) and allows us to model several realizations of stochastic fracture networks created using ADFNE (Alghalandis discrete fracture network engineering). The next section introduces the governing equations and the fracture model used to simulate these unconventional reservoirs with realistic natural fractures.

Natural Fracture Modeling with pEDFM

Although several models have been proposed to model fluid flow in naturally fractured reservoirs, we focus on EDFMs because they are able to account for the properties and orientation of each individual fracture in a reservoir. This section starts with an introduction of EDFM and ends with a discussion of its extension to a projection-based EDFM, which unlike EDFM is able to model low-conductivity fractures accurately. EDFM uses the concept of non-neighboring connections (NNCs) to couple the flow of fluids in a fracture cell to that of its host (or embedding) matrix cell. The coupling occurs by adding a q_i^{nnc} term to the semidiscrete form of the governing equation for compositional simulation (Eq. A-11), which is discussed in Appendix A, as follows:

$$\frac{V}{\Delta t} \left[\left(\phi \rho^l S^l X_i^l + \phi \rho^v S^v X_i^g \right)^{n+1} - \left(\phi \rho^l S^l X_i^l + \phi \rho^v S^v X_i^g \right)^n \right] + \text{div}(\rho^l X_i^l \bar{v}_i + \rho^v X_i^g \bar{v}^v)^{n+1} - (\rho^l X_i^l q^l + \rho^v X_i^g q^v)^{n+1} + q_i^{nnc} = R_i^{n+1}, \quad (1)$$

where q_i^{nnc} is the mass rate of component i that is exchanged through the NNC (in units of mass per time). It is given as:

$$q_i^{nnc} = \sum_{m=1}^{N_{nnc}} A_m^{nnc} \sum_{\alpha=1}^{n_p} \frac{k_m^{nnc} k_{r\alpha}}{\mu^\alpha} \rho^\alpha X_i^\alpha \left[\frac{(p^\alpha - \rho^\alpha g z) - (p^\alpha - \rho^\alpha g z)_m^{nnc}}{d_m^{nnc}} \right], \quad (2)$$

where subscript m is an index from 1 to the total number of non-neighboring connections for each cell (N_{nnc}). The flow potentials of a cell and its non-neighbouring cell are written as $(p^\alpha - \rho^\alpha g z)$ and $(p^\alpha - \rho^\alpha g z)_m^{nnc}$, respectively. To determine the transmissibility factor (T^{nnc}) between any pair of cells that are connected via non-neighboring connections, we need to estimate the area (A^{nnc}), permeability (k^{nnc}), and distance (d^{nnc}) of the non-neighboring connections. This transmissibility factor is given as:

$$T^{nnc} = \frac{k^{nnc} A^{nnc}}{d^{nnc}}. \quad (3)$$

The equations to estimate A^{nnc} , k^{nnc} , and d^{nnc} are different for different types of NNC. Moinfar et al. (2014) provides more details on these equations, as well as the expressions for the three types of NNCs in EDFM, which are shown in Fig. 4. The projection-based EDFM (Tene 2018) is based on a selection of neighboring projection matrix cells onto which each fracture cell is projected, in addition to the host matrix cell that contains the fracture cell. These selected neighboring cells are referred to as “projection matrix cells” and are selected based on the 3D projection algorithm presented in Olorode et al. (2020). The pEDFM extends the EDFM by adding two more NNC transmissibilities, which enables it to capture the effects of low-conductivity fractures. The first of these is the projection-matrix/fracture transmissibility (T_{pMF}), which is given as:

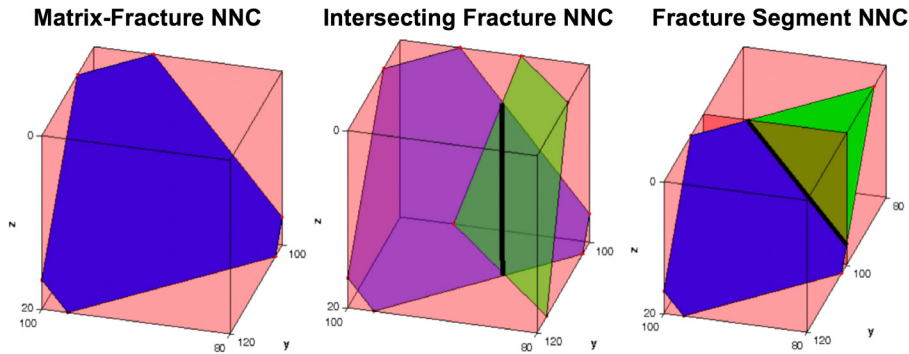


Fig. 4—This figure from Moinfar et al. (2014) illustrates (a) the NNC between a matrix and a fracture cell, (b) two fracture cells that belong to different fracture planes, and (c) two fracture cells that are part of the same fracture plane.

$$T_{pMF} = \frac{A_{\perp x} K_{pMF}}{d_{pMF}}, \quad (4)$$

where the harmonic average of the projection matrix and fracture cell permeabilities (K_{pMF}) is given as:

$$K_{pMF} = \frac{K_{pM} K_f}{K_{pM} + K_f}. \quad (5)$$

Here, d_{pMF} represents the distance between the centroid of the fracture and that of the projection cell, while $A_{\perp x}$ is the area of the fracture projection along each spatial dimension.

The projection-matrix/host-matrix transmissibility (T_{pMM}) is the second modification of the pEDFM, as is given as:

$$T_{pMM} = K \frac{A - A_{\perp x}}{\Delta \bar{x}_e}, \quad (6)$$

where $\Delta \bar{x}_e$ represents the cell size in all three spatial directions (for 3D systems), A is the area of the face between the projection and the host matrix cells, while $A_{\perp x}$ is the projection area. Olorode et al. (2020) provides further details on the 3D pEDFM algorithm, as well as its implementation for compositional reservoir simulation.

Fracture Network Connectivity Analysis

Considering the significant role natural fractures play in the flow of fluids in tight rocks, we perform a rigorous study of fracture network connectivity based on the dimensionless connectivity indices given in Haridy et al. (2019). The main objective of this study is to ensure an unbiased evaluation of the proposed SDEOR technology, regardless of the number, size, and other properties of the natural fractures simulated. Although Haridy et al. (2019) computed the different fracture indices for each cell in the reservoir, we extend this approach to compute the connectivity, crossing, and extended connectivity indices for the entire simulation domain as follows:

$$CI = \frac{\text{Total number of fracture-fracture intersections in the reservoir domain}}{\text{Total number of fractures in the reservoir}}, \quad (7)$$

$$CR_{i,j,k} = \frac{\text{Total number of matrix face-fracture intersections in } x, y, \text{ and } z \text{ directions}}{\text{Total number of fractures in the reservoir}}, \quad (8)$$

and

$$eCI_{i,j,k} = CR_{i,j,k} + CI. \quad (9)$$

In these equations, CI , $CR_{i,j,k}$, and $eCI_{i,j,k}$ are the connectivity, crossing, and extended connectivity indices, respectively. The subscripts i , j , and k are used to indicate that the crossing and extended connectivity indices are computed for the x -, y -, and z -directions. The connectivity index is computed by looping through all the fracture planes in the domain, counting the number of fracture-fracture intersections, and dividing that by the total number of fracture planes in the reservoir. The crossing index in the x -direction (CR_x) is computed by looping through all the cell faces in the x -direction, counting the total number of fractures that these faces, and dividing this by the total number of natural fractures in the reservoir simulation domain. The same procedure is repeated for CR_y and CR_z , except that we only use the y and z faces in these cases, respectively. The extended connectivity index ($eCI_{i,j,k}$) is computed as the summation of CI and $CR_{i,j,k}$.

The density of a fracture network can be represented by fracture intensity, which can be characterized using different measures, as in Niven and Deutsch (2010). In this work, fracture intensity (in units of 1/ft) is calculated by summing the areas of all the natural fractures in the reservoir (A_i), and dividing that by the bulk volume of the reservoir (V), as follows:

$$\text{Fracture Intensity} = \frac{\sum_{i=1}^n A_i}{V}. \quad (10)$$

The level of connectivity of a fracture network can be assessed by computing its “percolation threshold,” which is the interval above which the fracture network begins to contribute significantly toward the production from the fractured reservoir. The steps required to determine the percolation threshold for a fractured reservoir stimulated using the proposed SDEOR method are as follows:

1. Set up a reservoir model such that each matrix cell has dimensions exceeding the average length of any given natural fracture (NF) plane. **Table 2** and Tables B-1 and B-2 in Appendix B list the reservoir, binary interaction coefficients, and compositional data used in the model.
2. Increase the number of NFs in the reservoir, ranging from 8, 16, 32, 64, 128, 256, 512, 750, 1,024, to 1,500. A few of these realizations are shown in **Fig. 5**.
3. Compute CI , $eCI_{i,j,k}$, and fracture intensity (as in Eqs. 7, 9 and 10) for each realization.
4. Create a log-log plot of CI and $eCI_{i,j,k}$ against fracture intensity (**Fig. 6**).
5. Determine the percolation threshold at the fracture intensity range, where CI transitions from a nonlinear to a linear trend (Haridy et al. 2019) that increases monotonically. This range is delineated by the two dashed green lines in **Fig. 6**.

Parameters	SI Unit	Field Unit
Reservoir model dimensions	200×100×80 m	656.2×492.1×393.7 ft
Mesh size	5×5×(0.01 – 4) m	16.4×16.4×(0.016 – 13.1) ft
Initial reservoir pressure, p_i	3.93e+7 Pa	5,700 psia
Wellbore flowing pressure, p_{wf}	1.7237e+7 Pa	2,500 psia
Reservoir temperature	353 K	175°F
Matrix permeability, k_m	9.87e–18 m ²	1e–2 md
Matrix porosity, ϕ	0.07	0.07
Injection rate, q_{inj}	0.00615 m ³ /s	18,800 scf/D
Well radius, r_w	0.1 m	0.33 ft
# NFs (base case)	300	300
NF porosity, ϕ_{NF}	0.5	0.5
NF permeability, k_{NF}	9.87e–16 m ²	1 md
NF aperture, w_{NF}	3.05e–3 m	0.01 ft
# SD fractures	2	2
SD fracture porosity, ϕ_{SD}	0.33	0.33
SD fracture permeability, k_{SD}	9.87e–12 m ²	10 D
SD fracture aperture, w_{SD}	0.01 m	0.033 ft
SD fracture spacing	60 m	196.85 ft

Table 2—Reservoir input parameters.

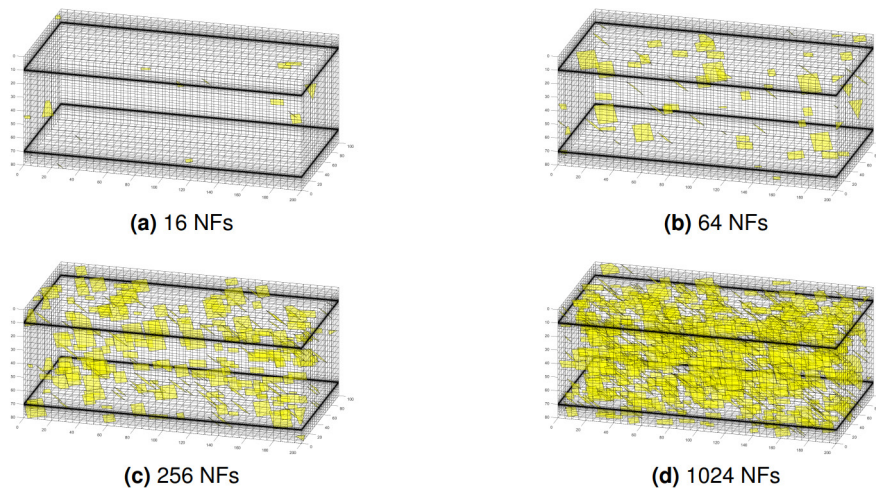


Fig. 5—The images show stochastic fracture networks with 16, 64, 256, and 1,024 natural fractures. Each image corresponds to one realization from a probabilistic distribution of the location, orientation, and size of the individual fractures that make up the fracture network with the specified number of fractures.

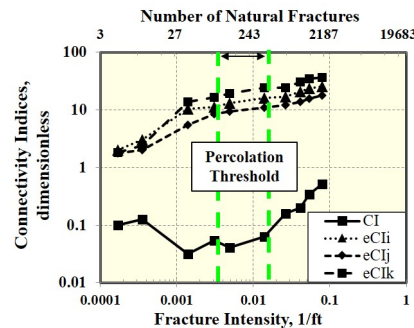


Fig. 6—A log-log plot of CI and $eCI_{i,j,k}$ against fracture intensities. Each point in this figure corresponds to the natural fracture networks shown in Fig. 5. The dashed green lines indicate the fracture intensity range that defines the percolation threshold, and the secondary X-axis shows the number of fractures that correspond to the fracture intensities on the primary X-axis.

Following the enumerated steps, the percolation threshold was determined to be at a fracture intensity between 0.005 and 0.014 ft^{-1} . This corresponds to having 70 to 260 natural fractures in the domain. At fracture intensity values above the percolation threshold, adding more stochastic fractures to the reservoir results in a significant change in oil production because of the increased fracture-fracture and fracture-matrix intersections. This change could be positive or negative, depending on the value of the fracture conductivity, as demonstrated in the subsequent subsections.

Evaluation of Primary Recovery from Single Slot-Drilled Fracture. To obtain useful insights on the role of gas injection in SDEOR technology in fractured tight rocks, we first simulate 8 years of primary oil production from a producing well that is completed using a slot-drill fracture near the bottom of the reservoir domain. These results provide a reference for the computation of the improved recovery obtained when gas is injected as proposed in SDEOR. **Table 2** summarizes the input parameters for the shale-oil reservoir simulated in this section, while Tables B-1 and B-2 in Appendix B summarize the compositional fluid data for the simple three-component mixture simulated in all but the last section of this paper. Although we use this simple mixture to facilitate the computationally expensive studies in this work, the final section provides a study of the applicability of the SDEOR technology using representative data for a Bakken shale-oil reservoir.

Fig. 7 presents the simulated oil RF and cumulative oil production against fracture intensity. The results show an exponential increase in cumulative oil production when the fracture intensity exceeds the percolation threshold. Although we only show results up to 0.1 ft^{-1} because of computational limitations, this exponential trend indicates that the cumulative production will increase considerably at higher values of fracture intensity. These results show that fractures contribute to an increase in production (when their number exceeds the percolation threshold) because the connected fractures provide a preferential path for the flow of fluids toward the production well. Below the percolation threshold, the contribution of the fractures to oil production is negligible because the fractures are scanty and disconnected from one another, as shown in **Figs. 5a and 5b**.

To explain why natural fractures do not contribute appreciably to production when the fracture connectivity is below the percolation threshold, we compute the connectivity indices in Eqs. 7 through 9 for each cell, as in Haridy et al. (2019). **Fig. 8** presents the $eCI_{k_{\text{cell}}}$ values for 16 and 512 natural fractures, which are respectively below and above the percolation threshold. The focus on the extended connectivity index in the z -direction is because the gravity drainage mechanism that dominates the SDEOR process acts in this direction. **Fig. 8a** indicates that the system with 16 natural fractures has limited fracture connectivity because of the zero values of eCI_k in most of the matrix cells. In contrast, **Fig. 8b** shows a system of 512 natural fractures, where the eCI_k values are greater than zero in several matrix

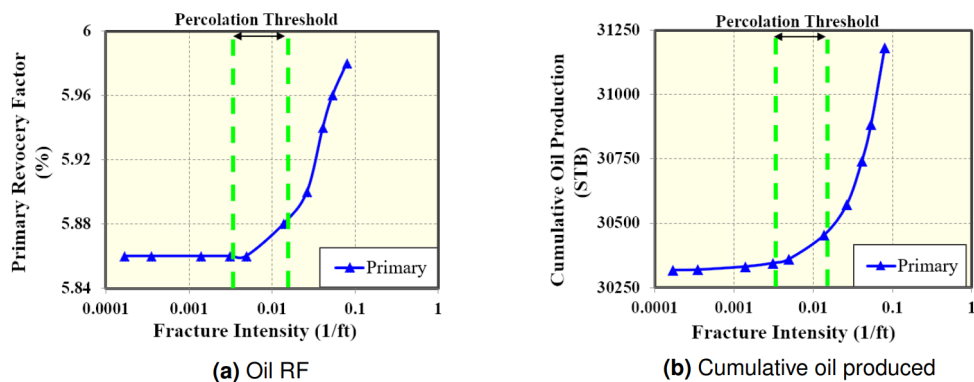


Fig. 7—The oil RF and cumulative oil production plots show increased production when the fracture intensity exceeds the percolation threshold. The dashed green lines indicate the percolation threshold.

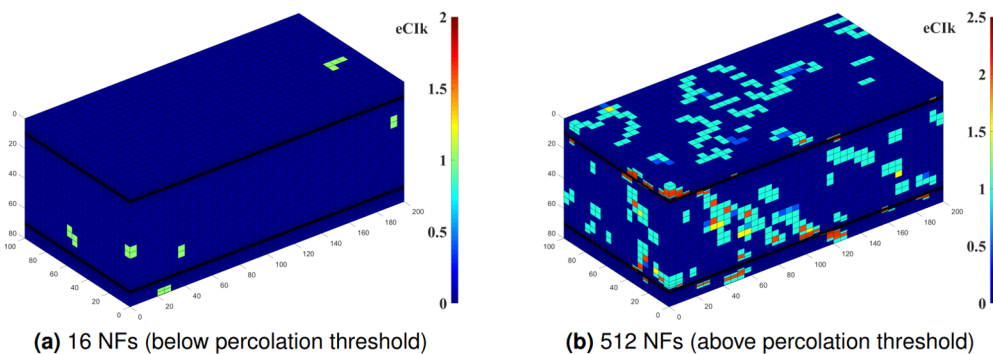


Fig. 8—The plots of eCI_k for each matrix cell show the poor and high fracture connectivities at (left) 16 and (right) 512 natural fractures, respectively.

cells. Therefore, the eCI_k profile provides a visual evidence for the significant connectivity of the fractures in reservoirs that have fracture intensities above the percolation threshold. It is also in agreement with the results presented previously in Fig. 7.

The next two sections focus on the evaluation of the near-term (8 years) and long-term (60 years) performance of SDEOR technology. The objective is to understand the physical mechanisms that control the short- and long-term performance of SDEOR in fractured tight rocks.

Short-Term Simulation Studies of the Application of SDEOR in Fractured Shale Oil Reservoirs

This subsection presents the results of the simulation of 8 years of methane gas injection into a slot-drilled fracture close to the top of the fractured reservoir while simultaneously producing oil from the slot-drilled fracture close to the bottom of the reservoir. To evaluate the robustness of the SDEOR technology in naturally fractured reservoirs, we simulated several realizations of the natural fracture network. This work also accounts for the fact that the permeability/conductivity of natural fractures could vary widely, ranging from sealing to highly conductive fractures, as shown in Table 3.

NF Network Type	NF Permeability (md)	NF Conductivity (md-ft)
Conductive	10	1
Sealing	1e-5	1e-6

Table 3—Different NF network conductivities for $k_m = 1e-2$ md.

Study of SDEOR Performance in Reservoirs with Only High-Conductivity Natural Fractures. Fig. 9 provides a box-plot that quantifies the uncertainty in the RF from SDEOR in a reservoir model with several realizations of only highly conductive natural fractures with a permeability of 10 md, as shown in Table 3. It shows that within the 8 years of simulated production, the RF remains above 13.64%, regardless of the number of fractures simulated. This indicates that the proposed SDEOR method is applicable regardless of the amount of conductive natural fractures in the reservoir. As the number of conductive fractures increases above the percolation threshold, the RF actually increases slightly. This is in agreement with the role of fractures in enhancing oil recovery in a gravity drainage process.

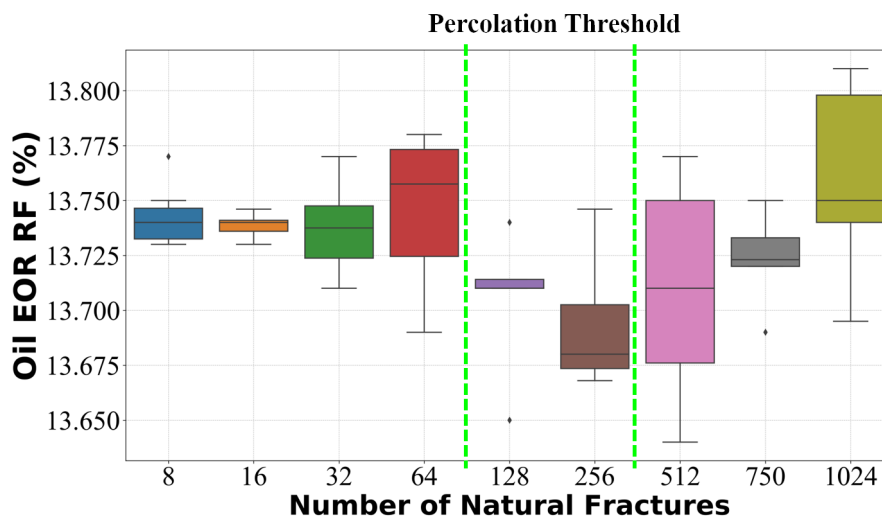


Fig. 9—These box plots indicate a small variation in the oil RF as the number of high-conductivity fractures increases from 8 to 1,024. Several realizations are simulated to quantify the uncertainty associated with different realizations of these conductive natural fracture networks.

Comparing the SDEOR RF to its corresponding value during primary recovery (which is 5.9% from **Fig. 7a**), it is clear that methane gas injection through the proposed technology results in a twofold increase in production over only 8 years of production.

To provide further insight into the SDEOR process in fractured shale-oil reservoirs, we present the profile of methane gas mole fraction in **Fig. 10**. The left image shows an almost piston-like displacement when the number of fractures in the domain are negligible (16 NFs in this case). However, when the number of natural fractures exceeds the percolation threshold, as in the image on the right, the injected methane gets diverted to various parts of the reservoir. Here, the network of 512 NFs transports the methane gas toward the top of the formation owing to buoyancy. This could lead to the formation of a secondary gas cap if the process is simulated for a much longer duration than the 8-year period simulated in this case. Subsequent sections involve simulating injection and production for 60 years, to study the long-term performance of the proposed SDEOR technology.

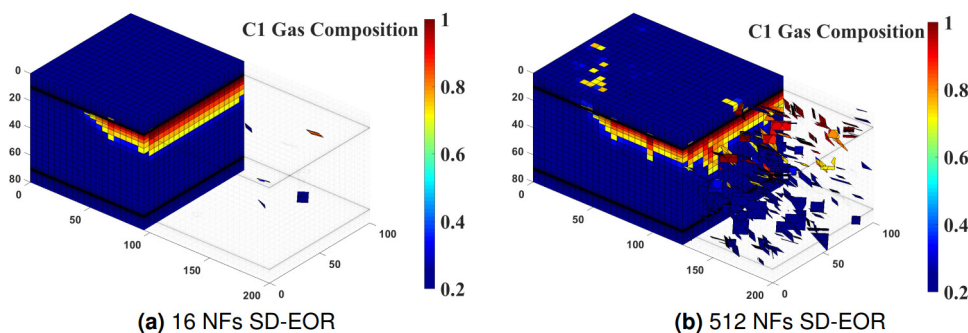


Fig. 10—Reservoir grid visualizations for C_1 gas composition by the end of 8 years of SDEOR simulation for conductive fracture networks: 16 NFs case (top) and 512 NFs case (bottom). Adding more NFs beyond the percolation threshold affects oil recovery under the SDEOR technology.

Study of SDEOR Performance in Reservoirs with Only Low-Conductivity Natural Fractures. Unlike the previous subsection, here we simulate several realizations of sealing fractures only with a permeability of $1e-5$ md, as shown in **Table 3**. **Fig. 11** provides a box-plot that shows how the oil RF for the SDEOR changes as the number of these sealing fractures increases. The results show that although the oil RF decreases slightly as the number of fractures increases, the proposed SDEOR technique still provides a twofold increase in recovery (in comparison to the primary RF of 5.9%) even with up to 1,024 sealing fractures.

Study of SDEOR Performance in Fractured Reservoirs. Considering that the fractures in shale-oil reservoirs were formed under different prevailing stress states and at different points in its geologic history, fracture conductivity typically varies over a wide range. Some fractures are conductive under the current stress state while others (that were previously active when formed) could be inactive or sealing in the prevailing stress state today. To account for this uncertainty in fracture conductivity, we simulate a case with 1,024 fractures, which have a mix of high- and low-conductivity fractures. The high-conductivity fractures have permeability values that are sampled from a normal distribution with a mean of 82 md and standard deviation of 52 md, while the low-conductivity fractures have a mean and standard deviation of 9 nd and 6 nd, respectively. The aperture (w_j) of each fracture in the network is computed from the cubic law for fracture permeability (K_f) as follows:

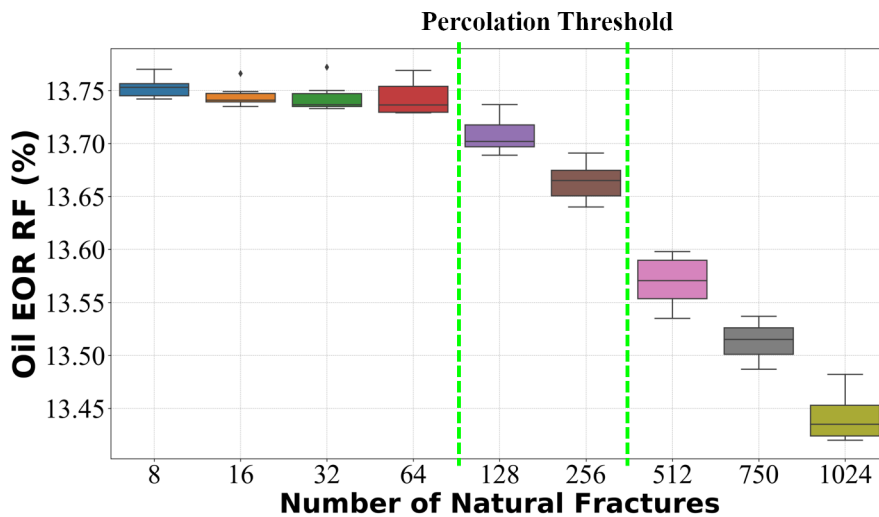


Fig. 11—These box plots quantify the effect of the uncertainty associated with different realizations of low-conductivity natural fracture networks. It shows a negligible decline in the RF as the number of sealing fractures increase.

$$w_f = \sqrt{12K_f} \quad (11)$$

Fig. 12 provides a box-plot that shows the oil RF for this case with mixed-conductivity fractures, in addition to the high- and low-conductivity fracture cases from the previous two subsections. In all three cases, the change in the RF for the SDEOR is minimal, indicating the robustness of this technology, regardless of the uncertainty in the fracture network. The next section focuses on the long-term performance of the SDEOR technology and shows simulation results for up to 60 years of production.

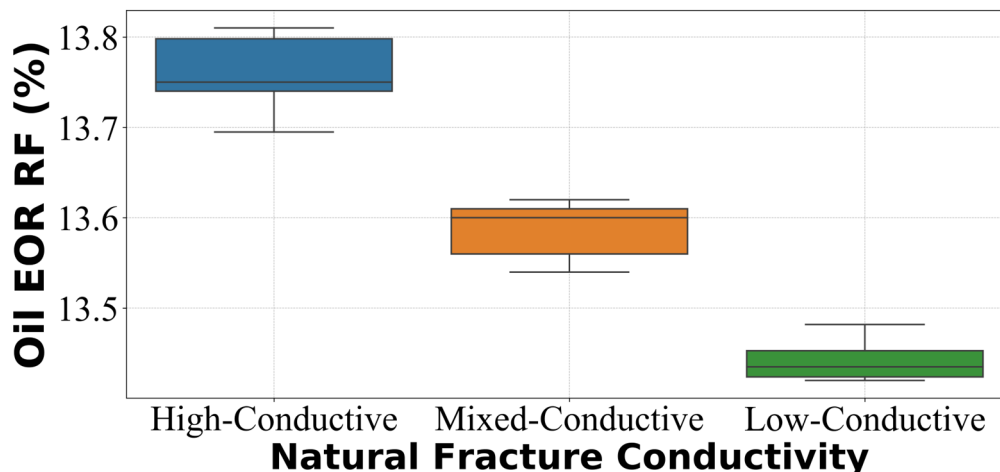


Fig. 12—These box plots indicate the robustness of the SDEOR technology in tight rocks with 1,024 fractures of high, low, and mixed conductivity values. For this extreme case of 1,024 NFs, the EOR RF only varies from 13.42 to 13.81% after 8 years of simulation.

Long-Term Simulation Studies of the Application of SDEOR

In this subsection, we assess the long-term performance of the proposed SDEOR technology in fractured shale-oil reservoirs by simulating up to 60 years of production. **Fig. 13** presents the plots of the cumulative oil and gas production for a base-case simulation with no natural fractures, a primary recovery case, as well as a case with 64 natural fractures (which is below the percolation threshold), an intermediate case of 256 natural fractures, and another with 1,024 fractures, which is well above the percolation threshold determined from the previous subsection. Compared to the primary recovery (green line), this figure shows that SDEOR results in a dramatic increase in cumulative oil production, regardless of the number of natural fractures in the reservoir. Performing the simulation for up to 60 years shows the long-term effectiveness of the proposed technology because the cumulative oil production increases at a constant rate for 30 years. It is worth noting that the injected gas does not break through before approximately 25 years of production (even with as many as 1,024 conductive natural fractures), and the cumulative gas production is the same in all SDEOR cases after 40 years of production. This is because of the role gravity plays in stabilizing the gas front and preventing early gas breakthrough through the fracture network. Unlike primary recovery from fractured rocks, where a higher number of conductive fractures typically yields more oil production, EOR from fractured rocks could result in lower oil production owing to earlier gas breakthrough. The highly conductive fractures created

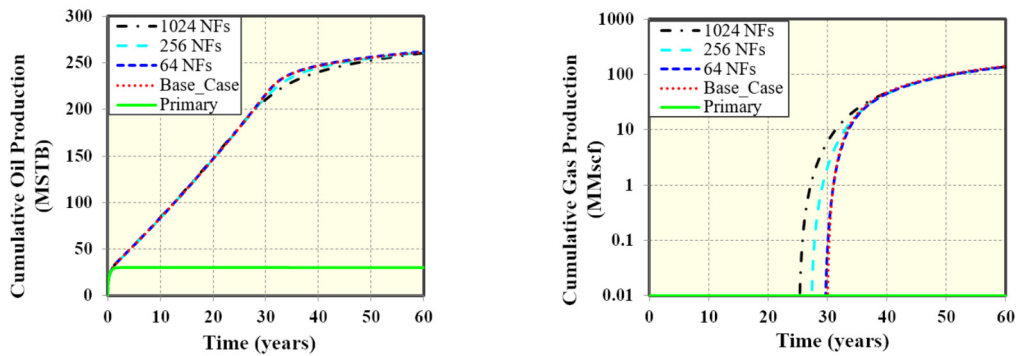


Fig. 13—These performance plots show the long-term effectiveness of the SDEOR technology, regardless of the presence of natural fractures. The results show that the oil production does not decline until after 30 years, and gas does not break through until after 25 years.

increase the anisotropy and heterogeneity of the system, resulting in a less piston-like displacement. This reduced sweep efficiency of the injected gas consequently yields earlier gas breakthrough at higher numbers of conductive fractures, as shown in **Fig. 13**. To clarify, the very small differences between the cumulative oil production results are inconclusive because of the uncertainties associated with the stochastic nature of the fracture networks.

To further show the robustness of SDEOR in the presence of natural fractures ranging from 0 to 1,024 and at different times in the life of the reservoir (at 8, 15, 30, and 60 years), we provide a plot of the SDEOR RF in **Fig. 14**. The nearly horizontal nature of this plot in the near and long term buttresses the conclusion that the recovery does not depreciate appreciably regardless of the presence or number of natural fractures in the reservoir. The red triangles plotted on the *y*-axis correspond to the base case with no natural fractures, which technically corresponds to a case with zero fracture intensity. **Fig. 15** shows the time evolution of the injected methane gas profile after 8, 15, 30, and 60 years in a reservoir with no natural fractures (base case) and another with 1,024 fractures. As time advances, the injected methane composition migrates toward the bottom producer, while some of this gas also moves to the top of the reservoir owing to buoyancy.

Table 4 summarizes the performance results of the SDEOR technology by comparing its RF with those from primary production. We also provide the change in RF (relative to primary recovery), as well as the IOR ratio, which can be as high as 8.58 after 60 years of production. To show the game-changing potential of the SDEOR technology in comparison to the application of CGEOR in use today, the next section provides a comparison of both technologies using the same reservoir model.

Gas Flooding Period (years)	Primary Oil RF	SDEOR Oil RF (1,024 NFs)	Increased Oil RF (%)	IOR Ratio
8	5.48	13.75	+8.27	2.37
15	5.48	22.15	+16.67	3.79
30	5.48	40.95	+35.47	6.94
60	5.48	50.14	+44.66	8.58

Table 4—SDEOR performance summary under different flooding periods in a reservoir with 1,024 conductive NFs.

Performance Comparison between CGEOR and SDEOR Technology. In this section, we compare the production performance of the proposed technology to the CGEOR method used in MSHF horizontal wells. The compositional fluid parameters and binary interaction coefficients used in both SDEOR and CGEOR models are provided in Tables B-1 and B-2 in Appendix B. To make a meaningful comparison between these two EOR technologies, we ensured that the total surface area of all the fractures in the CGEOR model shown in **Fig. 16** is equal to the area of one slot-drilled fracture shown in **Fig. 3**. The completion parameters for the slot-drilled fracture are presented in **Table 2**, while those for the MSHF wells are summarized in **Table 5**. Unlike the previous SDEOR simulation results presented in previous sections, this case was simulated at the same injection and flowing bottomhole pressures for the CGEOR case (in **Table 5**). Although methane gas is injected in both methods, SDEOR involves continuous gas injection, whereas in CGEOR, we simulated injection, soaking, and production for 25, 5, and 70 days, respectively. As reported in Jacobs (2019), this approach of minimizing the duration of injection and soaking is typically optimal in CGEOR. So, we use an optimal CGEOR operation schedule to avoid artificially making the CGEOR suboptimal.

Fig. 17 shows that the primary production from both slot-drilled and hydraulically fractured wells are practically identical because both methods model the same total fracture surface area. The other plots in this figure show that SDEOR yields much higher oil production and much less gas than CGEOR. The increased oil production could yield a sharp increase in the revenue from unconventional oil reservoirs, while the reduced gas production will minimize the costs of handling the associated gas. The slope of the left image changes after 2.3 years because the gas breaks through as shown in the right image. **Table 6** further quantifies the magnitude of the increase in recovery from the SDEOR in comparison to the CGEOR technology. It shows that over the first eight years of production, the proposed SDEOR technology yields 2.7 times more oil than the CGEOR method and 12 times more oil than primary oil production. This dramatic increase in the EUR from SDEOR in comparison to CGEOR could be attributed to the role gravity plays in stabilizing the gas front in

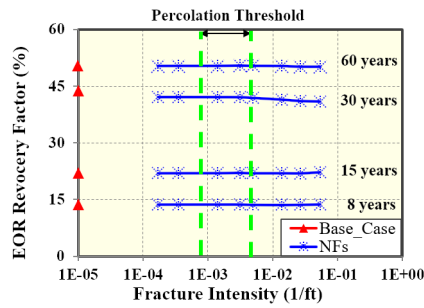


Fig. 14—The blue lines show that the EOR RF stays almost constant regardless of the fracture intensity, but increases over time as expected. The red triangles on the y-axis indicate the corresponding RF for a case with no fractures (zero fracture intensity). The percolation threshold is shown as the interval between the two green lines.

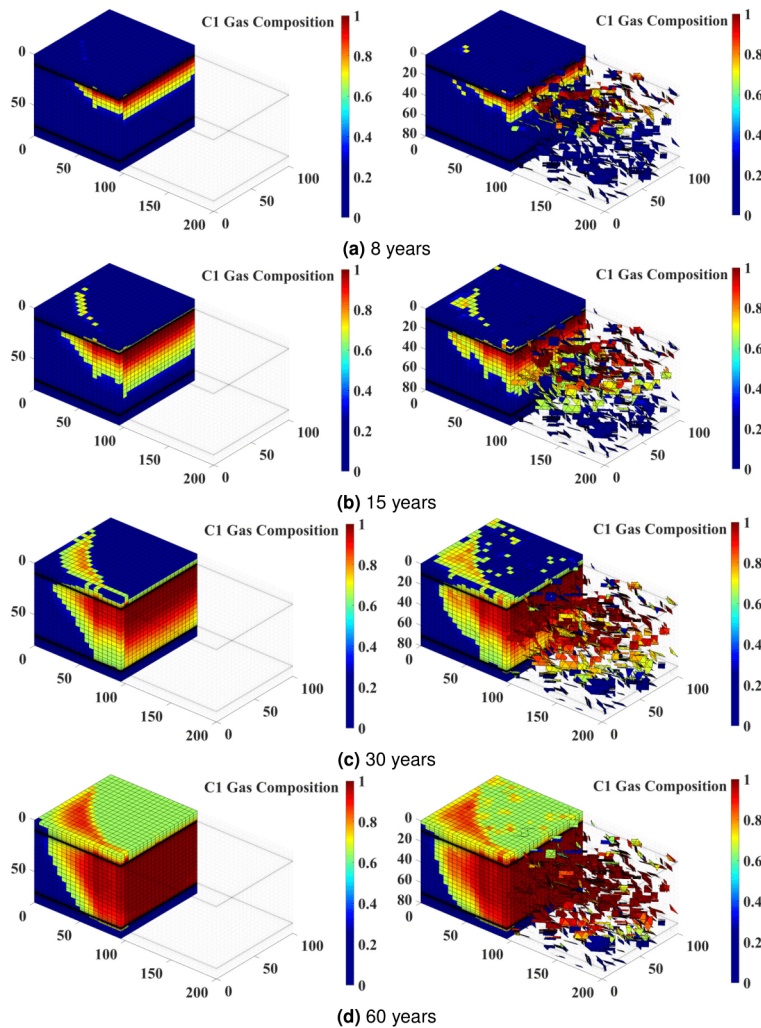


Fig. 15—These profiles show how the methane gas composition evolves for a base case without natural fractures (left column) and for a case with 1,024 conductive fractures (right column).

fractured unconventional reservoirs, as well as the fact that CGEOR only produces oil for a fraction of the life of the well and is either shut-in or injecting gas at other times.

Fig. 18 presents the methane gas profile after 8 years of simulation for both EOR techniques. The left image shows that the injected gas efficiently displaces the oil toward the slot-drilled fracture at the bottom of the reservoir. The red-colored cells delineate the portions of the reservoir that have been swept by the injected gas. The methane gas profile on the right in **Fig. 18** shows that some of the injected gas gets to the boundaries of the domain after 8 years of simulated production. **Fig. 19** presents slices of the domain in the x - and z -directions, and it shows that the injected gas travels horizontally in the reservoir as expected. The concentration of methane gas near the fracture surfaces results in high and low relative permeabilities to gas and oil, respectively. This consequently leads to a reduced flow of

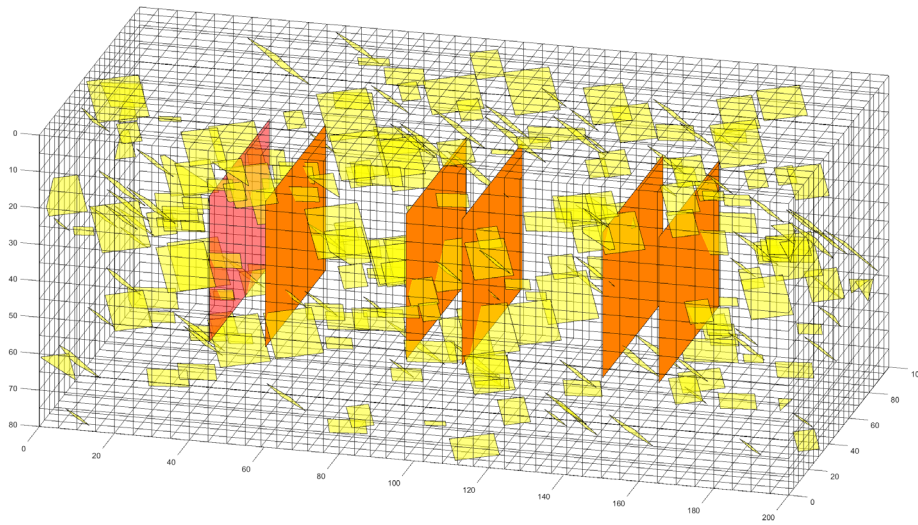


Fig. 16—Image shows the simulation domain for the CGEOR method. The natural fractures are shown as yellow planes, while the hydraulic fractures are shown as red vertical planes.

Parameters	SI Unit	Field Unit
Injection pressure, P_i	4.6195e+7 Pa	6,700 psia
Wellbore flowing pressure, P_{wf}	1.7237e+7 Pa	2,500 psia
Fracture half-length, x_f	30 m	98.4252 ft
Fracture width, w_f	0.003 m	0.00984 ft
Cluster spacing	15 m	49.21 ft
Fracture spacing	37.5 m	123.03 ft
Fracture permeability, k_f	9.87 e-13 m ²	1e3 md
Fracture porosity, ϕ_{frac}	0.5	0.5
Well radius, r_w	0.1 m	0.32 ft
Injection period (Jacobs 2019)	25 days	25 days
Soaking period	5 days	5 days
Production period	70 days	70 days
Cycle duration	100 days	100 days

Table 5—Input parameters for CGEOR in MSHF completion.

oil and an increased flow of gas toward the hydraulically fractured well. This is a fundamental limitation of the CGEOR method, which significantly curtails oil production later in the life of the well. The use of a pair of slot-drilled fractures in the SDEOR technology helps

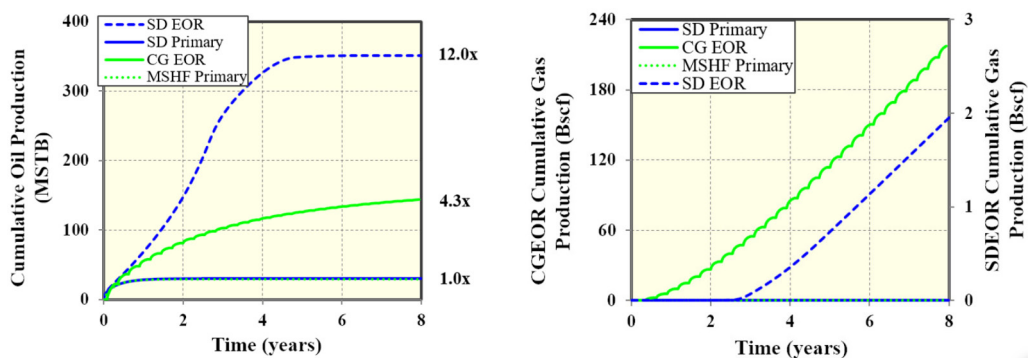


Fig. 17—The results show that SDEOR yields 2.7 times more oil than CGEOR, and half as much of associated gas production. The primary recovery from the slot-drilled and MSHF wells match because the total fracture area is the same in both cases.

Recovery Mechanism	Oil RF (%)	EUR (MSTB)	IOR Ratio
Primary	6	30	N/A
CGEOR	26	131	4.3
SDEOR	70	352	12

Table 6—Performance comparison between SDEOR and CGEOR after 8 years for a simple fluid mixture.

avoid this limitation, resulting in a continued increase in cumulative oil production, as shown in Fig. 17. Conversely, in CGEOR, the cumulative oil production flattens out because more gas is produced instead of oil as the huff 'n' puff process continues.

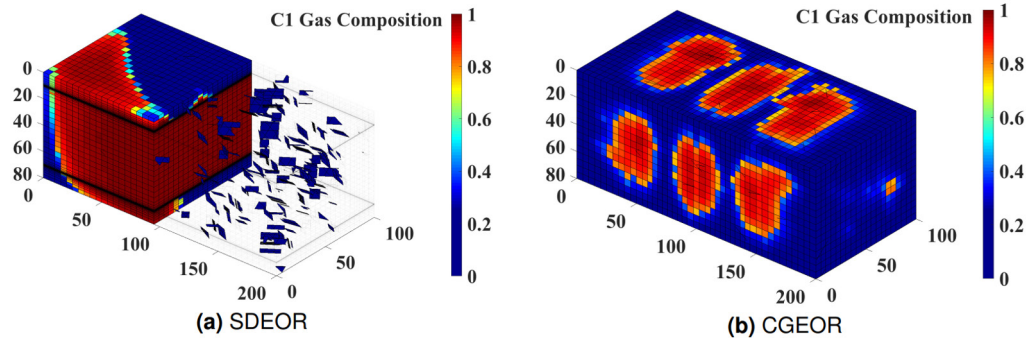


Fig. 18—Left image shows the methane gas profile after 8 years of simulated SDEOR while right image shows the corresponding methane profile from the CGEOR method.

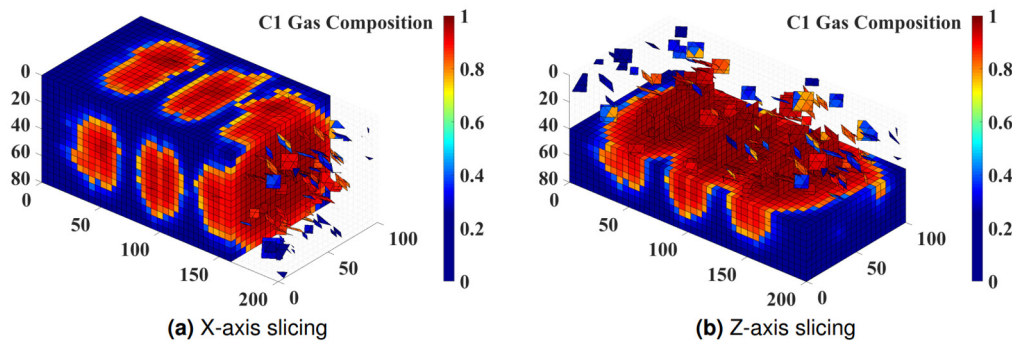


Fig. 19—Left image shows the profile for the methane mole fraction, with the last 8 cells in the x-direction taken out, while the right image cuts out half of the matrix cells above the middle of the reservoir. It shows that the methane gas saturates the pore volume in the vicinity of the hydraulic fracture clusters, leading to the limited performance of the CGEOR method.

Evaluation of the Recovery Mechanisms in SDEOR

In this section, we study the role of different recovery mechanisms in the proposed SDEOR technology using the reservoir and fluid input parameters in Table 2 and Tables B-1 and B-2 in Appendix B, respectively. An understanding of the physical mechanisms that control the performance of the SDEOR process could facilitate the design of an efficient field implementation of this technology. Here, we focus on three main recovery mechanisms:

1. Pressure-driven recovery
2. Gravity drainage
3. Oil viscosity reduction

The Role of the Pressure Difference between the Injector and Producer. The goal in this section is to study the effect of the pressure difference between the injector and producer (ΔP_{diff}) on the oil recovery from SDEOR. As shown in Fig. 20, we ran four simulation cases at a fixed flowing bottomhole pressure of 2,500 psia but at injection pressures (P_{inj}) ranging from 5,700 to 7,700 psi. This yielded the four injection pressures shown in the figure. The cumulative oil production plots in Fig. 20a shows that although we produce more oil earlier in the well life at higher injection pressures, the cumulative oil production converges to the same value. As expected, the case with the lower injection pressure yields lower cumulative gas production, which could be important in controlling the amount of associated gas produced from the proposed technology.

It is worth noting that while the pressure difference in the SDEOR technology acts continuously between the injector and producer, in CGEOR, the effect of a pressure increase is only felt during the injection and soaking period. This could also contribute to the lower oil production observed from our simulations of the CGEOR method.

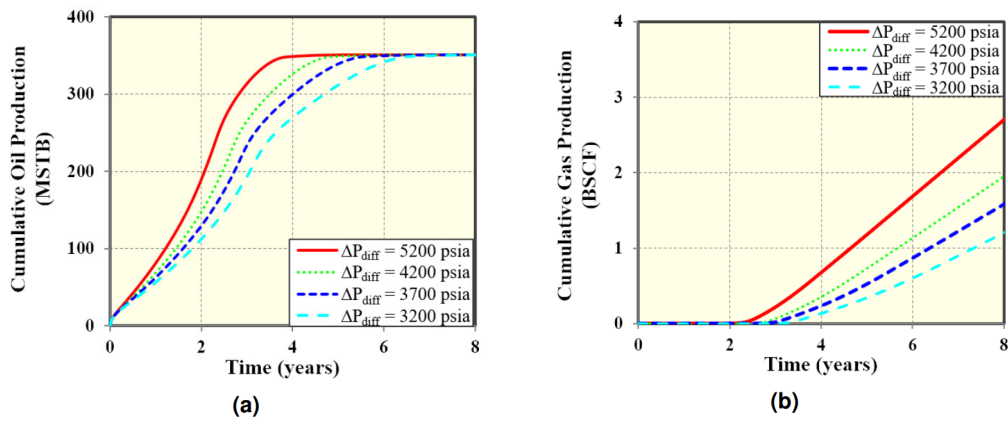


Fig. 20—Performance plots show the role of the pressure difference between the injector and producer in the SDEOR technology. Figs. 20a and 20b present the plots of cumulative oil and gas production.

The Role of Gravity Drainage. Here, we demonstrate the role of gravity drainage in the SDEOR technology by simply turning gravity off and on, and comparing the corresponding oil production from both cases. Our simulation results show that gravity results in more oil recovery at higher matrix permeability values and in systems with dense networks of high-conductivity fractures. Considering that shale-oil reservoirs are typically naturally fractured and with low matrix permeabilities, we present the results for a shale reservoir with a matrix permeability of 50 μd and 512 natural fractures (which is above the percolation threshold). The simulation results given in Fig. 21 shows that gravity accounts for 20% of the oil production after after 30 years of simulated production. This effect could be even more significant if the simulation is run for a longer duration, or if more and larger subvertical fractures are simulated. In Fig. 22, we show the profile for the mole fraction of methane gas (C_1) after 30 years when gravity is turned on (left images) and when it is turned off (right images). A comparison of the methane-gas composition profiles after 15 and 30 years indicates that gravity helps stabilize the injected gas front and delays the breakthrough of the gas at the producer, as confirmed by the cumulative gas production presented in Fig. 20b. These results indicate that the role of gravity in the proposed SDEOR technology could be the game changer in shale plays like the Bakken, which are known to have low matrix permeabilities and complex network of fractures. In such systems, the CGEOR method has not been successful, as discussed in Kuuskraa et al. (2020). This could be attributed to the predominantly horizontal flow expected during CGEOR through nearly vertical fractures. However, in the vertical flow expected in SDEOR, gravity appears to curtail early gas production through the high-conductivity fracture flow paths by the buoyancy of the injected gas. Fig. 22 also shows that the gas rises to the top of the reservoir when gravity is turned on but does not otherwise.

The Role of Oil Viscosity Reduction. To evaluate the role of oil viscosity in the proposed SDEOR technology, we again simulate the SDEOR technology by injecting at a constant q_{inj} of 18.8 Mscf/D and a P_{wf} of 2,500 psia for 30 years. We then compute the surface oil viscosity shown in Fig. 23, using the Lohrenz-Bray-Clark compositional viscosity model (Lohrenz et al. 1964). The simulated viscosity of the oil produced at the surface is observed to decrease from an initial value of 0.017 cp to 0.0158 cp (−7.6% change) after 30 years. We also observe from Fig. 24 that the viscosity of the oil left in the reservoir decreases during gas injection. This is because the injected methane gas appears to mix with the oil phase, making it less viscous. Oil phase mobility ($\frac{K_o}{\mu_o}$) increases as its viscosity decreases, and this makes it flow more easily toward the bottom producer in the SDEOR technology. Although the decrease in the oil-phase viscosity is rather small because the commercial shale oil plays are usually volatile oils, higher viscosity mixtures have been shown to yield more significant viscosity changes during miscible gas injection (Zou and Schechter 2017; Hao et al. 2020).

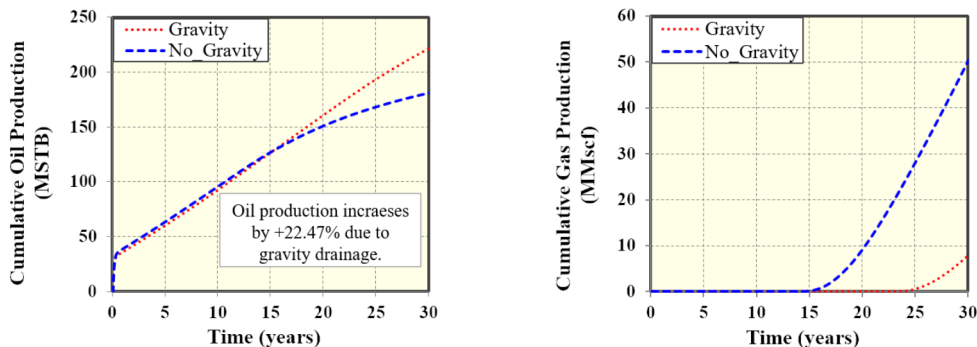


Fig. 21—Performance plots for the cases with and without gravity demonstrates that gravity plays a significant role in the SDEOR technology.

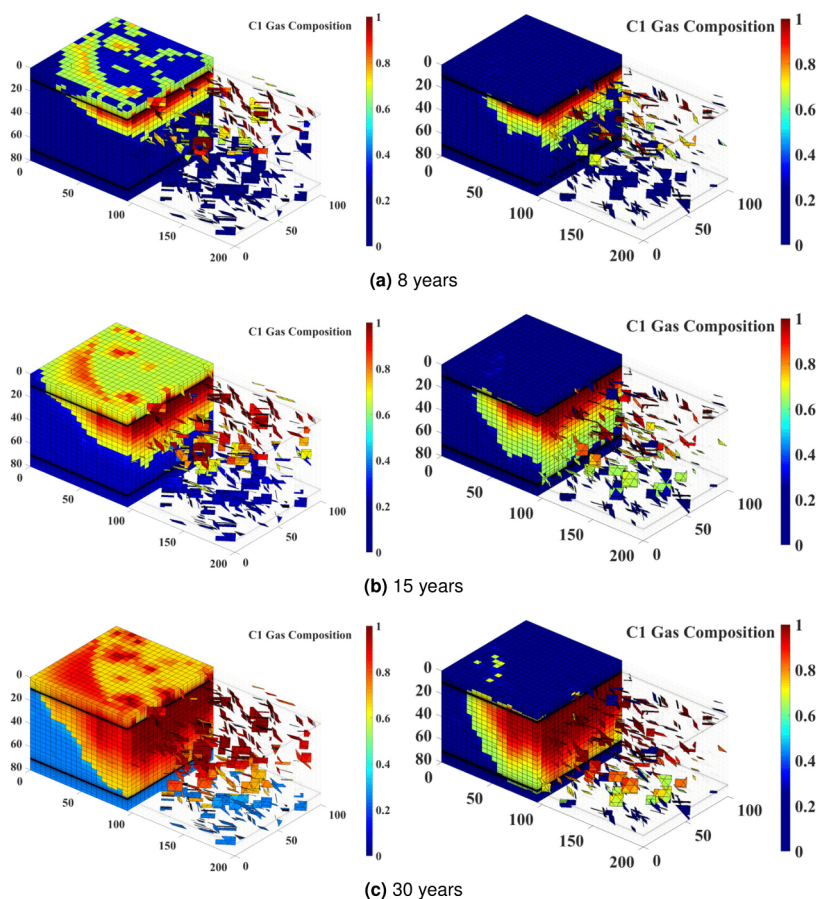


Fig. 22—Left and right images show the profile of methane gas mole fraction with and without gravity, respectively. Left images show that gravity helps delay the breakthrough of the injected methane gas in comparison to the case where gravity is ignored.

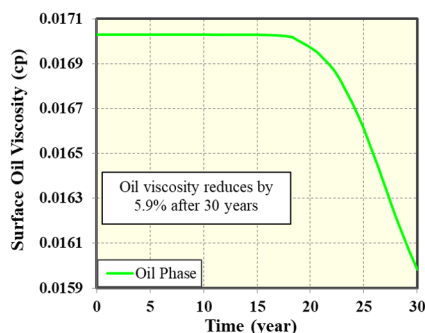


Fig. 23—Plot of surface oil viscosity shows that the oil gets less viscous as the injected methane gas mixes with the oil in the reservoir.

SDEOR Application to Eagle Ford and Bakken Shale Plays

In this section, we numerically evaluate the application of SDEOR in comparison to CGEOR in actual shale plays. To ensure that the CGEOR cases simulated are not curtailed by suboptimal operating conditions (in comparison to SDEOR), we will simulate the cyclic injection of methane gas under efficient operating conditions as follows:

1. Use optimum field injection, soaking, and production durations of 60, 14, and 180 days (2, 0.5, and 6 months), respectively (Kuuskraa et al. 2020).
2. Operate at P_{wf} above P_b to prevent the vaporization of the oil and ensure optimum CGEOR RF (Sun et al. 2019).
3. Start CGEOR after the cumulative oil production from primary recovery flattens out.

In the next two subsections, we present the results from the simulation of the Eagle Ford and Bakken shale formations. In both cases, we simulate primary production for 3 years, after which we model both CGEOR and SDEOR for 8 more years.

Eagle Ford Shale. To model a volatile oil Eagle Ford shale reservoir, we use the fluid composition data presented in Tables B-3 and B-4 in Appendix B. Most of the reservoir input parameters used are given in **Table 2**, but to model a representative Eagle Ford shale

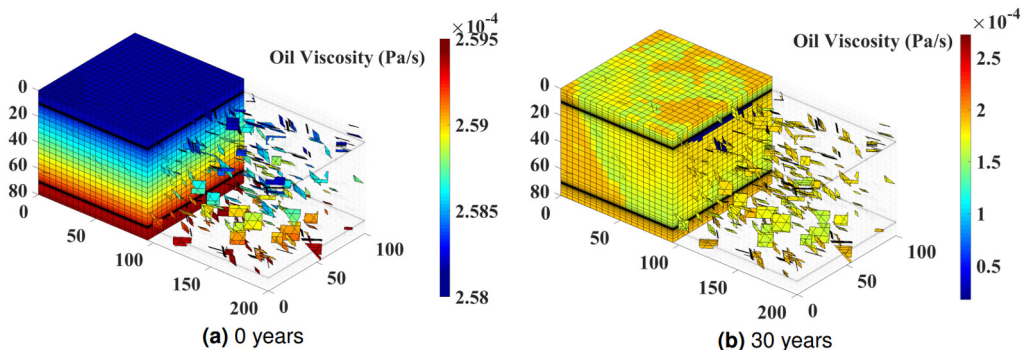


Fig. 24—Images show in-situ oil phase viscosity at the beginning (left) and after 30 years (right) of simulating the SDEOR technology. In-situ oil viscosity decreases as injected gas continuously mixes with the oil in the reservoir.

reservoir, we use P_i , P_{wf} , q_{inj} , and k_m values of 7,000 psia, 2,500 psia (above $P_b = 1,560$ psia), 400 Mscf/D, and $1 \mu d$, respectively, for both SDEOR and CGEOR cases. We do not simulate any natural fracture in this case because Raterman et al. (2018) did not observe any natural fractures from their extensive sampling of a stimulated rock volume by drilling multiple lateral wellbores through a region around a stimulated Eagle Ford shale well. **Fig. 25** compares the production performance of the SDEOR technology to the CGEOR method. It shows that SDEOR produces 3.8 times more oil than CGEOR after 11 years of simulated production. The flattening of the slope of the SDEOR cumulative oil production (dotted blue line) corresponds to the time the injected gas breaks through into the bottom producer after 6 years of production. This is confirmed in the right plot in **Fig. 25**, which shows that the gas production from SDEOR is negligible until it breaks through when most of the oil is already recovered. This observation indicates that the production of associated gas is typically negligible while most of the oil is being recovered during SDEOR, which will minimize the costs associated with gas handling in the surface facilities. As explained in the previous section, the reduction in gas production until gas breaks through is because of the role of gravity in stabilizing the gas front in SDEOR from fractured reservoirs.

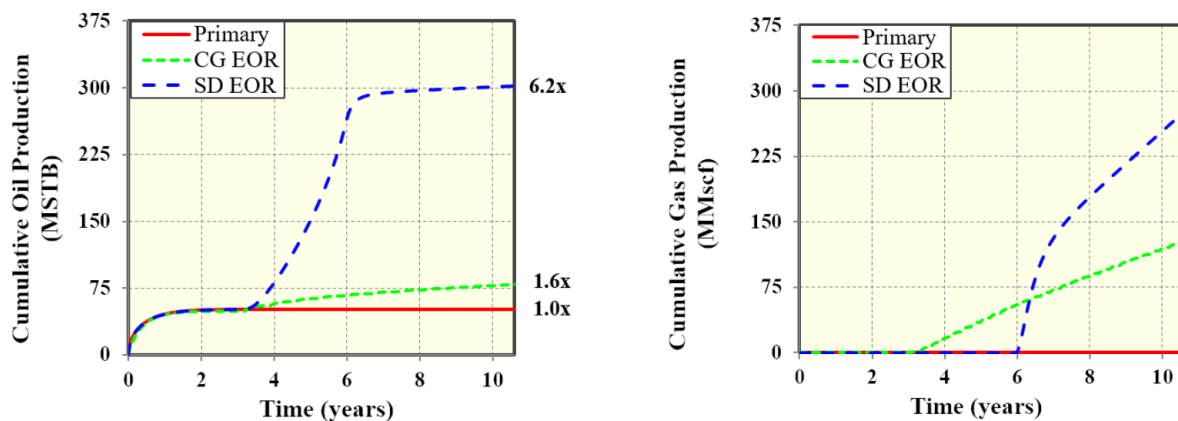


Fig. 25—Performance plots show a comparison of the cumulative oil (left) and gas (right) production from primary production, CGEOR, and SDEOR from a representative Eagle Ford shale oil well. The results show that SDEOR yields 3.8 times more oil than CGEOR.

The dramatic increase in oil recovery from SDEOR in comparison to CGEOR even in shale reservoirs with little or no fractures shows the applicability in such shale plays. In the next subsection, we focus on shale plays such as the Bakken shale (which has lots of complex fractures), where CGEOR has not been successful at increasing the recovery significantly.

Bakken Shale. To model a volatile oil Bakken shale reservoir, we use the fluid composition data presented in Tables B-5 and B-6. Most of the reservoir input parameters used are given in **Table 2**, but to model a representative Bakken shale reservoir, we use P_i , P_{wf} , q_{inj} , and k_m values of 6,700 psia, 3,000 (above $P_b = 1,640$ psia), 60 Mscf/D, and $10 \mu d$, respectively, for both SDEOR and CGEOR cases. We simulate 150 subvertical natural fracture planes with 1.5 md-ft conductivity, dip ranging from 60° to 90° (with a mean of 80°), and dip direction between $N50^\circ W$ and $S40^\circ E$, as interpreted from the formation microimager logs (Sturm and Gomez 2009). **Fig. 26** compares the production performance of the SDEOR technology to the CGEOR method. It shows that SDEOR produces 3.2 times more oil than CGEOR after 11 years of simulated production. Additionally, CGEOR yields a considerable amount of associated gas (cumulative gas production of 15.2 MMscf), whereas the SDEOR technology does not yield any gas production during the 11 years of production because the injected gas is yet to break through at the bottom producer. This result points to the flexibility in designing the SDEOR technology to optimize the duration of oil production before gas breakthrough, by modifying the injection rates or pressure based on the permeability and thickness of the shale formation.

Table 7 summarizes the results of the simulated recoveries from both the Eagle Ford and Bakken shale plays using SDEOR and CGEOR. The IOR ratios for the CGEOR method lies within the published range for the Eagle Ford (1.34–1.62) and Bakken (1.11–1.41) shale plays (Kuuskraa et al. 2020). The consistently superior recovery from the proposed SDEOR technology (at least three times higher

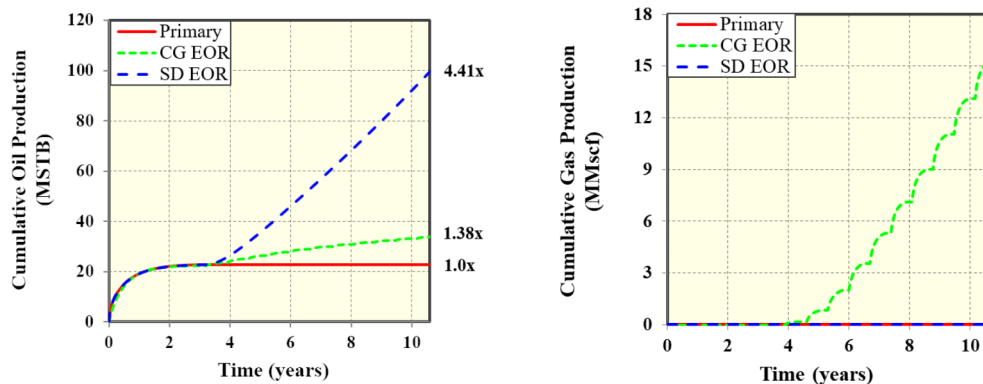


Fig. 26—Performance plots show a comparison of the cumulative oil (left) and gas (right) production from primary production, CGEOR, and SDEOR from a representative Bakken shale oil well. The results show that SDEOR yields 3.2 times more oil than CGEOR.

recovery than the CGEOR method in both shale plays) indicates its potential to be a game changer in the recovery of oil from shale-oil reservoirs.

Shale Formation	Recovery Mechanism	Oil RF (%)	EUR (MSTB)	IOR Ratio
Eagle Ford shale	Primary	10.7	49.2	N/A
	CGEOR	17.1	77.9	1.6
	SDEOR	66.0	302.8	6.2
Bakken shale	Primary	5.0	24.1	N/A
	CGEOR	6.8	33.2	1.38
	SDEOR	21.8	106.2	4.41

Table 7—Incremental oil recovery in shale formations from SDEOR and CGEOR.

In the next two subsections, we focus on the application of the SDEOR technology in the Bakken shale, where CGEOR field pilots have been reported to be unsuccessful and operationally challenging because the injected gas disperses quickly into the natural fracture network without soaking in effectively into the oil-charged matrix (Kuuskraa et al. 2020). The goal is to study the performance of the SDEOR technology in Bakken shale-oil reservoirs under the following unfavorable EOR conditions (Pospisil et al. 2020):

1. The presence of natural fracture networks at low and high conductivities.
2. Operating at P_{wf} (1,000 psia) below both P_b (1,640 psia) and the minimum miscibility pressure for different solvents used (such as CH_4 , N_2 , flue gas, and CO_2).

Study of SDEOR Performance in Bakken Shales with Different Fracture Conductivities. Here, we simulate the injection of methane into a Bakken shale oil reservoir at a constant rate of 20 Mscf/D for 30 years. To quantify the increase in recovery via SDEOR, we also simulate primary production without gas injection. The SDEOR cases studied include a base case without natural fractures, one with 1,024 conductive natural fractures, and another with 1,024 nonconductive (NC) natural fractures. We use as many as 1,024 natural fractures to ensure that the fracture network connectivity exceeds the percolation threshold. **Fig. 27** presents the cumulative oil and gas production plots for these three cases, as well as the reference case under primary recovery. These results show that the proposed SDEOR technology increases the oil recovery by a factor of at least 4 in all three cases studied. **Fig. 28** shows the profile for methane-gas composition for these three SDEOR cases. It shows that the inclusion of the stochastic fracture networks in the reservoir domain slightly decreases the sweeping efficiency as seen in the slight distortion of the more stable gas front in the case with no fractures (**Fig. 28a**). Nonetheless, the proposed SDEOR technology still yields over four times more oil in the Bakken shale regardless of the presence of a large number of conductive or nonconductive/sealing fractures. These results confirm the applicability of this technology in unfractured shale-oil reservoirs like the Eagle Ford shale play (Raterman et al. 2018) and in densely fractured reservoirs like the Bakken shale play (Kuuskraa et al. 2020).

Study of SDEOR Performance with Different Injectants. In this subsection, we simulate the injection of different gases (CH_4 , N_2 , flue gas, and CO_2) into the Bakken shale using the proposed SDEOR technology. **Fig. 29** shows a comparison of the cumulative oil (left) and gas (right) production when these different gases are injected, while **Table 8** summarizes these results and provides the molecular weight of each of the injected gases. The dotted lines in the figure correspond to the results when gravity is turned off, while the solid lines of the same color are the results for the corresponding case with gravity turned on. The difference between the cases with and without gravity is more significant for the lighter gases (methane and nitrogen) than the heavier gases. The comparison of the results of the different injectants (with gravity) also indicates that the recovery increases as the molecular weight of the injected gas decreases. This could be attributed to the increased role of gravity when lighter gases are injected because the density difference between injected gas and the original reservoir fluid (buoyancy effects) is higher. It is worth noting from the last column in **Table 8** that although all gases were simulated at the same value of injection rate, the corresponding injection pressure for each case was observed to be different. This is expected considering that in the Peaceman well model, the injection rate is inversely proportional to the viscosity but directly proportional

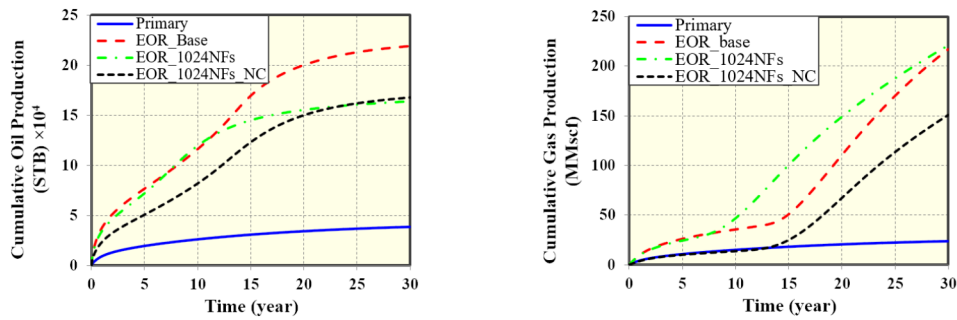


Fig. 27—Results indicate the robustness of the proposed technology as it produces at least four times more oil than primary recovery regardless of the number of sealing or conductive fractures in the reservoir.

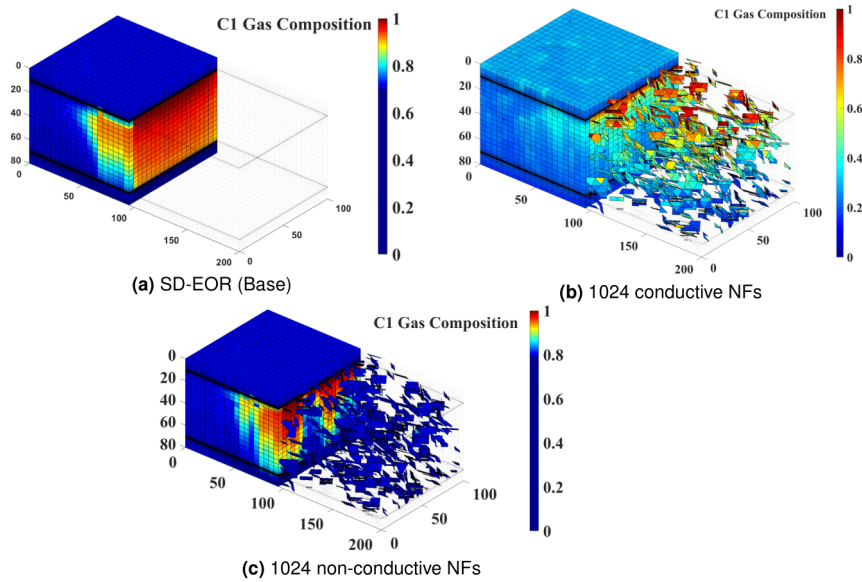


Fig. 28—Methane gas composition profile after 30 years of simulated SDEOR for (a) a base case without natural fractures, (b) a case with 1,024 conductive fractures, and (c) a case with 1,024 nonconductive fractures. Adding natural fractures beyond the percolation threshold slightly distorts the gas front.

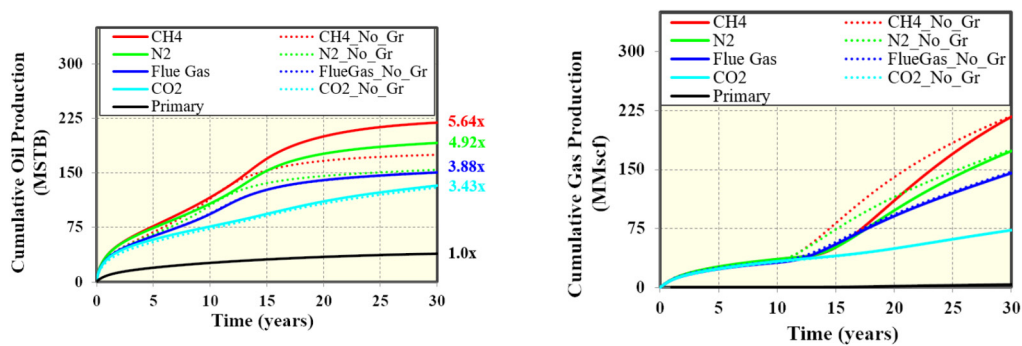


Fig. 29—Performance plots show that methane gas injection recovers more oil when compared with the injection of the other heavier gases.

to the pressure difference between the cell and injection pressures. So, as the gas viscosity increases for the denser gases, the pressure difference will increase, resulting in lower injection pressures at a fixed value of cell pressure. This explains the lower values of ΔP_{diff} for denser gases because $\Delta P_{diff} = P_{inj} - P_{wf}$ and P_{wf} is fixed.

Solvent Method	Molecular Weight (kg/kg-mol)	Oil RF (%)	Increased Oil RF (%)	IOR Ratio	ΔP_{diff} (psia)
CH ₄	16.04	37.70	29.45	5.64	950
N ₂	28.01	32.85	24.6	4.92	890
Flue gas (25% CO ₂ +75% N ₂)	32.01	31.79	23.54	3.88	850
CO ₂	44.01	29.40	21.15	3.43	770

Table 8—Results of SDEOR with different gas injectants.

Conclusions

This work presents a novel EOR technology for unconventional reservoirs based on gas injection into a horizontal slot-drilled fracture near the top of the reservoir and oil production from another slot-drilled fracture near the bottom. Our simulation results show that the proposed technology could outperform the CGEOR method by a factor of at least 3. From the numerical studies of the physical mechanisms that control the proposed technology, we conclude that the dramatic increase in recovery is because of the following:

1. The continuous injection and production in the SDEOR technology curtails the significant reduction in relative oil permeability because of the increasing gas saturation near the well during the cyclic gas injection in CGEOR.
2. The SDEOR technology allows continuous production for 100% of the well life, whereas in CGEOR, production is halted during the injection and soaking periods.
3. The SDEOR technology is designed to take advantage of gravity in stabilizing the flow through the fracture network unlike CGEOR, which involves a preferential flow through the poorly known fracture network.

The simulation results presented show that the proposed technology yields much higher oil recoveries regardless of the presence/absence of natural fractures of high, low, or intermediate conductivity. Our simulation of SDEOR in the Bakken shale (which has not been successfully enhanced using CGEOR) shows an IOR of at least 4 when we simulated the injection of four different gases (CH₄, N₂, flue gas, and CO₂).

Although the focus of this work is to numerically evaluate our novel SDEOR technology in comparison to the CGEOR method, it is worth mentioning that the slot-drill fracturing technology is yet to be tested in the field. Future studies will focus on an experimental validation of the high recoveries from the proposed technology. The idea is to provide a proof-of-concept that could lead to the field testing of the proposed technology.

Nomenclature

$A_{if\perp x}$ = Area of fracture projections along each dimension L², m²

A_{ij}^p = projection area, L², m²

A^{nnc} = area of a non-neighboring connection, L², m²

d^{nnc} = non-neighboring connection distance, L, m

K_f = fracture permeability, L², m²

k_m = matrix permeability, L², m²

k^{nnc} = permeability of a non-neighboring connection, L², m²

K_i = vapor-liquid equilibrium constant for component i

R = residual, M⁻¹ L⁻³, kg⁻¹ m⁻³

S^α = saturation of phase, α

t = time, T, seconds

T_i = half-transmissibility, L³, m³

T^{nnc} = transmissibility factor for an NNC, L³, m³

q^α = Volumetric flow rate of phase α , L³/T, m³/s

\bar{x}_e = gridblock sizes in the x -, y -, and z - directions, L, m

\bar{x} = X, Y, and Z coordinates, L, m

x_i = mole fraction of component, i in the liquid phase

X_i^α = mass fraction of component i in phase, α

Y_i = mass fraction of component, i in the gas phase

y_i = mole fraction of component, i in the gas phase

Z_i = overall mass fraction of component, i

ϕ = porosity

ρ = density, M/L³, kg/m³

f = fracture

m = matrix

MM = interaction between two different host matrix cells

pMF = interaction a projection matrix and a fracture cell

i, j = cell indices

if = interaction between matrix cell, i and fracture cell, f

α = fluid phase

$k + 1$ = current timestep

nnc = non-neighbouring connections

Acknowledgments

The authors would like to acknowledge Bin Wang for assisting in the fracture connectivity studies. This work was facilitated by the use of the software packages available in the Craft and Hawkins Department of Petroleum Engineering at Louisiana State University (LSU) and the computational resources at the LSU Center for Computation and Technology (CCT).

References

- Apiwathanasorn, S. and Ehlig-Economides, C. 2012. Evidence of Reopened Microfractures in Production Data Analysis of Hydraulically Fractured Shale Gas Wells. Paper presented at the SPE Canadian Unconventional Resources Conference, Calgary, Alberta, Canada, 30 October–1 November. SPE-162842-MS. <https://doi.org/10.2118/162842-MS>.
- Carter, E. E. 2011. Method and Apparatus for Increasing Well Productivity. US Patent App. 13/130,579.
- Coats, K. H. 1979. An Equation of State Compositional Model. *SPE J.* **20** (5): 363–376. SPE-8284-PA. <https://doi.org/10.2118/8284-PA>.
- Coleman, I. J. K. and Hester, N. C. 2010. Drilling and Opening Reservoir Using an Oriented Fissure to Enhance Hydrocarbon Flow and Method of Making. US Patent 7,647,967.
- Dahaghi, A. K. 2010. Numerical Simulation and Modeling of Enhanced Gas Recovery and CO₂ Sequestration in Shale Gas Reservoirs: A Feasibility Study. Paper presented at the SPE International Conference on CO₂ Capture, Storage, and Utilization, New Orleans, Louisiana, USA, 10–12 November. SPE-139701-MS. <https://doi.org/10.2118/139701-MS>.
- Du, F. and Nojabaei, B. 2019. A Review of Gas Injection in Shale Reservoirs: Enhanced Oil/Gas Recovery Approaches and Greenhouse Gas Control. *Energies* **12** (12): 2355. <https://doi.org/10.3390/en12122355>.
- Eshkalak, M. O., Al-Shalabi, E. W., Sanaei, A. et al. 2014. Enhanced Gas Recovery by CO₂ Sequestration versus Re-Fracturing Treatment in Unconventional Shale Gas Reservoirs. Paper presented at the Abu Dhabi International Petroleum Exhibition and Conference, Abu Dhabi, UAE, 10–13 November. SPE-172083-MS. <https://doi.org/10.2118/172083-MS>.
- Farrar, R. B., Mayercheck, W. D., and Bockosh, G. R. 1991. Method of Mining a Mineral Deposit Seam, US Patent 299/18; 299/35.
- Firoozabadi, A. 2015. *Thermodynamics and Applications of Hydrocarbon Energy Production*. New York, USA: McGraw Hill Professional.
- Ganjdanesh, R., Yu, W., Fiallos Torres, M. X. et al. 2019. Huff-N-Puff Gas Injection for Enhanced Condensate Recovery in Eagle Ford. Paper presented at the SPE Annual Technical Conference and Exhibition, Calgary, Alberta, Canada, 30 September–2 October. SPE-195996-MS. <https://doi.org/10.2118/195996-MS>.
- Grinstaff, G., Barden, C., Miller, J. et al. 2020. Evaluation of Eagle Ford Cyclic Gas Injection EOR: Field Results and Economics. Paper presented at the SPE Improved Oil Recovery Conference, Virtual, 31 August–4 September. SPE-200427-MS. <https://doi.org/10.2118/200427-MS>.
- Hakso, A. and Zoback, M. 2019. The Relation between Stimulated Shear Fractures and Production in the Barnett Shale: Implications for Unconventional Oil and Gas Reservoirs. *Geophysics* **84** (6): B461–B469. <https://doi.org/10.1190/geo2018-0545.1>.
- Hao, M., Liao, S., Yu, G. et al. 2020. Performance Optimization of CO₂ Huff-n-Puff for Multifractured Horizontal Wells in Tight Oil Reservoirs. *Geofluids* **2020**: 1–13. <https://doi.org/10.1155/2020/8840384>.
- Haridy, M. G., Sedighi, F., Ghahri, P. et al. 2019. Comprehensive Study of the Oda Corrected Permeability Upscaling Method. Paper presented at the SPE/IATMI Asia Pacific Oil & Gas Conference and Exhibition, Bali, Indonesia, 29–31 October. SPE-196399-MS. <https://doi.org/10.2118/196399-MS>.
- Hoffman, B. T. 2018. Huff-N-Puff Gas Injection Pilot Projects in the Eagle Ford. Paper presented at the SPE Canada Unconventional Resources Conference, Calgary, Alberta, Canada, 13–14 March. SPE-189816-MS. <https://doi.org/10.2118/189816-MS>.
- Hoffman, B. T. and John, G. E. 2016. Improved Oil Recovery IOR Pilot Projects in the Bakken Formation. Paper presented at the SPE Low Perm Symposium, Denver, Colorado, USA, 5–6 May. SPE-180270-MS. <https://doi.org/10.2118/180270-MS>.
- Hughes, J. D. 2018. Shale Reality Check. Santa Rosa, California, USA: Post Carbon Institute.
- Hurd, R. L. 1980. Method and Apparatus for Deep Mining Using Chain Driven in Fixed Direction. US Patent 4,232,904.
- Jacobs, T. 2019. Shale EOR Delivers, So Why Won't the Sector Go Big? *J Pet Technol* **71** (5): 37–41. SPE-0519-0037-JPT. <https://doi.org/10.2118/0519-0037-JPT>.
- Karimi-Fard, M. and Firoozabadi, A. 2001. Numerical Simulation of Water Injection in 2D Fractured Media Using Discrete-Fracture Model. Paper presented at the SPE Annual Technical Conference and Exhibition, New Orleans, Louisiana, USA, 30 September–3 October. SPE-71615-MS. <https://doi.org/10.2118/71615-MS>.
- Kerr, E., Venepalli, K. K., Patel, K. et al. 2020. Use of Reservoir Simulation to Forecast Field EOR Response - An Eagle Ford Gas Injection Huff-N-Puff Application. Paper presented at the SPE Hydraulic Fracturing Technology Conference and Exhibition, The Woodlands, Texas, USA, 4–6 February. SPE-199722-MS. <https://doi.org/10.2118/199722-MS>.
- Kim, J.-G. and Deo, M. D. 2000. Finite Element, Discrete-Fracture Model for Multiphase Flow in Porous Media. *AIChE J* **46** (6): 1120–1130. <https://doi.org/10.1002/aic.690460604>.
- Kim, T. H., Park, S. S., Lee, K. S. et al. 2015. Modeling of CO₂ Injection Considering Multi-Component Transport and Geomechanical Effect in Shale Gas Reservoirs. Paper presented at the SPE/IATMI Asia Pacific Oil & Gas Conference and Exhibition, Nusa Dua, Bali, Indonesia, 20–22 October. SPE-176174-MS. <https://doi.org/10.2118/176174-MS>.
- Kuuskräa, V., Murray, B., and Petrusak, R. 2020. Increasing Shale Oil Recovery and CO₂ Storage with Cyclic CO₂ Enhanced Oil Recovery. Arlington, Virginia, USA: Advanced Resources International, Inc. <https://bit.ly/3414f1u>.
- Li, L. and Lee, S. H. 2008. Efficient Field-Scale Simulation of Black Oil in a Naturally Fractured Reservoir Through Discrete Fracture Networks and Homogenized Media. *SPE Res Eval & Eng* **11** (4): 750–758. SPE-103901-PA. <https://doi.org/10.2118/103901-PA>.
- Lie, K.-A. 2019. *An Introduction to Reservoir Simulation Using MATLAB/GNU Octave: User Guide for the MATLAB Reservoir Simulation Toolbox (MRST)*. Cambridge, UK: Cambridge University Press. <https://doi.org/10.1017/9781108591416>.
- Lohrenz, J., Bray, B. G., Clark, C. R. et al. 1964. Calculating Viscosities of Reservoir Fluids From Their Compositions. *J Pet Technol* **16** (10): 1171–1176. SPE-915-PA. <https://doi.org/10.2118/915-PA>.
- Moinfar, A., Varavei, A., Sepehrnoori, K. et al. 2014. Development of an Efficient Embedded Discrete Fracture Model for 3D Compositional Reservoir Simulation in Fractured Reservoirs. *SPE J.* **19** (2): 289–303. SPE-154246-PA. <https://doi.org/10.2118/154246-PA>.
- Moridis, G., Reagan, M. et al. 2020. Evaluation of the Effectiveness of Continuous Gas Displacement for EOR in Hydraulically Fractured Shale Reservoirs. Paper presented at the SPE Latin American and Caribbean Petroleum Engineering Conference, Virtual, 27–31 July. SPE-198999-MS. <https://doi.org/10.2118/198999-MS>.
- Møyner, O., Tchelepi, H. et al. 2017. A Multiscale Restriction-Smoothed Basis Method for Compositional Models. Paper presented at the SPE Reservoir Simulation Conference, Montgomery, Texas, USA, 20–22 February. SPE-182679-MS. <https://doi.org/10.2118/182679-MS>.
- Niven, E. B. and Deutsch, C. V. 2010. Relating Different Measures of Fracture Intensity. CCG Annual Report-Paper 103. Centre for Computational Geostatistics.

- Oduwo, T. O., Moridis, G. J., Blasingame, T. A. et al. 2014. Evaluation of Well Performance for the Slot-Drill Completion in Low- and Ultralow-Permeability Oil and Gas Reservoirs. *SPE J.* **19** (5): 748–760. SPE-164547-PA. <https://doi.org/10.2118/164547-PA>.
- Olorode, O., Wang, B., Rashid, H. U. et al. 2020. Three-Dimensional Projection-Based Embedded Discrete-Fracture Model for Compositional Simulation of Fractured Reservoirs. *SPE J.* **25** (4): 2143–2161. SPE-201243-PA. <https://doi.org/10.2118/201243-PA>.
- Pankaj, P., Mukisa, H., Solovyeva, I. et al. 2018. Enhanced Oil Recovery in Eagle Ford: Opportunities Using Huff-n-Puff Technique in Unconventional Reservoirs. Paper presented at the SPE Liquids-Rich Basins Conference - North America, Midland, Texas, USA, 5–6 September. SPE-191780-MS. <https://doi.org/10.2118/191780-MS>.
- Peng, D.-Y. and Robinson, D. B. 1976. A New Two-Constant Equation of State. *Ind Eng Chem Fund* **15** (1): 59–64. <https://doi.org/10.1021/i160057a011>.
- Pospisil, G., Weddle, P., Strickland, S. et al. 2020. Report on the First Rich Gas EOR Cyclic Multiwell Huff N Puff Pilot in the Bakken Tight Oil Play. Paper presented at the SPE Annual Technical Conference and Exhibition, Virtual, 26–29 October. SPE-201471-MS. <https://doi.org/10.2118/201471-MS>.
- Pruess, K. and Narasimhan, T. N. 1982. A Practical Method for Modeling Fluid and Heat Flow in Fractured Porous Media. *SPE J.* **25** (1): 14–26. SPE-10509-PA. <https://doi.org/10.2118/10509-PA>.
- Rassenfoss, S. 2017. Shale EOR Works, But Will It Make a Difference? *J Pet Technol* **69** (10): 34–40. SPE-1017-0034-JPT. <https://doi.org/10.2118/1017-0034-JPT>.
- Rateman, K. T., Farrell, H. E., Mora, O. S. et al. 2018. Sampling a Stimulated Rock Volume: An Eagle Ford Example. *SPE Res Eval & Eng* **21** (4): 927–941. SPE-191375-PA. <https://doi.org/10.2118/191375-PA>.
- Shafiei, A., Dusseault, M. B., Kosari, E. et al. 2018. Natural Fractures Characterization and In Situ Stresses Inference in a Carbonate Reservoir—An Integrated Approach. *Energies* **11** (2): 312. <https://doi.org/10.3390/en11020312>.
- Sturm, S. D. and Gomez, E. 2009. Role of Natural Fracturing in Production from the Bakken Formation, Williston Basin North Dakota. Paper presented at the AAPG Annual Convention and Exhibition, Denver, Colorado, USA, 7–10 June.
- Sun, J., Zou, A., Schechter, D. et al. 2016. Experimental and Numerical Studies of CO₂ EOR in Unconventional Liquid Reservoirs with Complex Fracture Networks. Paper presented at the SPE Improved Oil Recovery Conference, Tulsa, Oklahoma, USA, 11–13 April. SPE-179634-MS. <https://doi.org/10.2118/179634-MS>.
- Sun, R., Yu, W., Xu, F. et al. 2019. Compositional Simulation of CO₂ Huff-n-Puff Process in Middle Bakken Tight Oil Reservoirs with Hydraulic Fractures. *Fuel* **236**: 1446–1457. <https://doi.org/10.1016/j.fuel.2018.09.113>.
- Tene, M. 2018. *Algebraic Multiscale Framework for Fractured Reservoir Simulation*. PhD Thesis, Delft University of Technology. <https://doi.org/10.4233/uuid:0ce45ddb-4932-4808-aa92-bd13deb85fa9>.
- Tene, M., Bosma, S. B. M., Al Kobaisi, M. S. et al. 2017. Projection-Based Embedded Discrete Fracture Model (PEDFM). *Adv Water Resour* **105**: 205–216. <https://doi.org/10.1016/j.advwatres.2017.05.009>.
- Warren, J. E. and Root, P. J. 1963. The Behavior of Naturally Fractured Reservoirs. *SPE J.* **3** (3): 245–255. SPE-426-PA. <https://doi.org/10.2118/426-PA>.
- Yu, W., Lashgari, H., Sepehrnoori, K. et al. 2014. Simulation Study of CO₂ Huff-n-Puff Process in Bakken Tight Oil Reservoirs. Paper presented at the SPE Western North American and Rocky Mountain Joint Meeting, Denver, Colorado, USA, 17–18 April. SPE-169575-MS. <https://doi.org/10.2118/169575-MS>.
- Yu, W., Lashgari, H. R., Wu, K. et al. 2015. CO₂ Injection for Enhanced Oil Recovery in Bakken Tight Oil Reservoirs. *Fuel* **159**: 354–363. <https://doi.org/10.1016/j.fuel.2015.06.092>.
- Yu, W., Zhang, Y., Varavei, A. et al. 2019. Compositional Simulation of CO₂ Huff 'n' Puff in Eagle Ford Tight Oil Reservoirs With CO₂ Molecular Diffusion, Nanopore Confinement, and Complex Natural Fractures. *SPE Res Eval & Eng* **22** (2): 492–508. SPE-190325-PA. <https://doi.org/10.2118/190325-PA>.
- Zhu, P., Balhoff, M. T., and Mohanty, K. K. 2017. Compositional Modeling of Fracture-to-Fracture Miscible Gas Injection in an Oil-Rich Shale. *J Pet Sci Eng* **152**: 628–638. <https://doi.org/10.1016/j.petrol.2017.01.031>.
- Zou, A. and Schechter, D. 2017. Investigation of the Oil Recovery Mechanism during Laboratory CO₂ EOR Experiments with Unconventional Shale Cores through Compositional Simulation. Paper presented at the Carbon Management Technology Conference, Houston, Texas, USA, 17–20 July. CMTC-486243-MS. <https://doi.org/10.7122/486243-MS>.
- Zuloaga, P., Yu, W., Miao, J. et al. 2017. Performance Evaluation of CO₂ Huff-n-Puff and Continuous CO₂ Injection in Tight Oil Reservoirs. *Energy* **134**: 181–192. <https://doi.org/10.1016/j.energy.2017.06.028>.

Appendix A—Governing Equations for Compositional Reservoir Simulation

Without accounting for the presence of natural fractures, the governing equations for the mass conservation of each hydrocarbon component, i , in the liquid (l) and vapor (v) phases is given as:

$$\frac{\partial}{\partial t} (\phi [\rho^l S^l X_i^l + \rho^v S^v X_i^g]) + \nabla \cdot (\rho^l X_i^l \vec{v}^l + \rho^v X_i^g \vec{v}^v) - (\rho^l X_i^l q^l + \rho^v X_i^g q^v) / V = 0. \quad (\text{A-1})$$

Similarly, the mass conservation equation for water (w) in the aqueous phase is given as:

$$\frac{\partial}{\partial t} (\phi \rho^w S^w) + \nabla \cdot (\rho^w \vec{v}^w) - \rho^w q^w / V = 0, \quad (\text{A-2})$$

where ϕ , ρ^α , S^α , and q^α represent the matrix porosity, mass density, saturation, and volumetric withdrawal/injection rate of phase α , respectively. The symbols X_i^l and X_i^g represent the mass fractions of component i in the liquid and vapor phases, while \vec{v}^l and \vec{v}^v are the Darcy velocities for the liquid and vapor hydrocarbon phases, respectively. Note that the division of the source/sink term in Eqs. A-1 and A-2 by bulk volume, V is needed for dimensional consistency.

We obtain the phase velocities in Eqs. A-1 and A-2 from Darcy's equation as follows:

$$\vec{v}^\alpha = -\mathbf{K} \frac{k^\alpha(S)}{\mu^\alpha} (\nabla p^\alpha - \rho^\alpha g \nabla z), \quad (\text{A-3})$$

where μ^α and \mathbf{K} represent the phase viscosity and absolute matrix permeability, respectively. In the natural variables composition approach (Coats 1979), which is used in this work, the primary variables are pressure, vapor, and liquid composition of all but the last component, and water saturation (p , $x_1^l, x_1^g, \dots, x_{n-1}^l, x_{n-1}^g$, and S_w), respectively. The auxiliary thermodynamic equations and constraints needed for compositional simulation are summarized as follows:

$$f_i^g(p, T, y_1, \dots, y_n) - f_i^l(p, T, x_1, \dots, x_n) = 0, \quad \text{for } i \in 1, \dots, n_c, \quad (\text{A-4})$$

$$z_i - Lx_i - (1 - L)y_i = 0, \quad \text{for } i \in 1, \dots, n_c, \quad (\text{A-5})$$

$$\sum_{i=1}^{n_c} x_i = 1, \quad \text{for } i \in 1, \dots, n_c, \quad (\text{A-6})$$

$$\sum_{i=1}^{n_c} y_i = 1, \quad \text{for } i \in 1, \dots, n_c, \quad (\text{A-7})$$

$$S^w + S^l + S^v = 1.0. \quad (\text{A-8})$$

In these equations, f_i^g and f_i^l are the fugacities of each component in the gas and liquid phases, respectively. Eq. A-4 ensures that the fugacity of each component in the vapor phase is equal to that of the same component in the liquid phase (which is required at chemical equilibrium), Eq. A-5 ensures that the sum of the number of moles of each component in the liquid and gas phases is equal to its corresponding overall composition, while Eqs. A-6, A-7, and A-8 ensure that all mole fractions and saturations sum up to one.

We use the Peng-Robinson equation of state (Peng and Robinson 1976) to compute the fugacities and phase compressibility factors (Z^g and Z^l). Firoozabadi (2015) provides more details on the equation of state, flash procedure, and the equations to compute the fugacities and compressibility factors. To solve the continuous equations in Eqs. A-1 and A-2 numerically, we first perform a temporal discretization using the backward Euler scheme as follows:

$$\frac{1}{\Delta t} \left[\left(\phi \rho^l S^l X_i^l + \phi \rho^v S^v X_i^g \right)^{n+1} - \left(\phi \rho^l S^l X_i^l + \phi \rho^v S^v X_i^g \right)^n \right] + \nabla \cdot (\rho^l X_i^l \vec{v}^l + \rho^v X_i^g \vec{v}^v) - (\rho^l X_i^l q^l + \rho^v X_i^g q^v) / V = R_i, \quad (\text{A-9})$$

$$\frac{1}{\Delta t} \left[(\phi \rho^w S^w)^{n+1} - (\phi \rho^w S^w)^n \right] + \nabla \cdot (\rho^w \vec{v}^w) - \rho^w q^w / V = R^w. \quad (\text{A-10})$$

In the above equations, $n + 1$ represents the current timestep, while n represents the previous timestep. Note that all other terms without these superscripts are evaluated at the current timestep. We then proceed to discretize the flux terms in space using the finite volume method with two-point flux approximation. The two-point flux approximation method involves integrating Eqs. A-9 and A-10 over a control volume, after which the divergence theorem is applied. In this work, we use the discrete divergence (*div*) and gradient (*grad*) operators, which are discussed in Lie (2019) and implemented as functions in the MATLAB Reservoir Simulation Toolbox. The resulting discretized form of Eqs. A-9 and A-10 can be written as:

$$\frac{V}{\Delta t} \left[\left(\phi \rho^l S^l X_i^l + \phi \rho^v S^v X_i^g \right)^{n+1} - \left(\phi \rho^l S^l X_i^l + \phi \rho^v S^v X_i^g \right)^n \right] + \text{div}(\rho^l X_i^l \vec{v}^l + \rho^v X_i^g \vec{v}^v)^{n+1} - (\rho^l X_i^l q^l + \rho^v X_i^g q^v)^{n+1} = R_i^{n+1}, \quad (\text{A-11})$$

and

$$\frac{V}{\Delta t} \left[(\phi \rho^w S^w)^{n+1} - (\phi \rho^w S^w)^n \right] + \text{div}(\rho^w \vec{v}^w)^{n+1} - (\rho^w q^w)^{n+1} = R_w^{n+1}, \quad (\text{A-12})$$

where

$$\vec{v}^\alpha = -T_{ik} \lambda_\alpha^{n+1} [\text{grad}(p_\alpha^{n+1}) - \rho_\alpha^{n+1} g \text{grad}(z)], \quad (\text{A-13})$$

$$T_{ik} = \left[T_{i,k}^{-1} + T_{k,i}^{-1} \right]^{-1}, \quad (\text{A-14})$$

and

$$T_{i,k} = A_{i,k} \mathbf{K}_i \frac{\vec{c}_{i,k} \cdot \vec{n}_{i,k}}{|\vec{c}_{i,k}|^2}. \quad (\text{A-15})$$

Here, V and $A_{i,k}$ refer to the cell volumes and face areas, respectively. The symbol, $\vec{n}_{i,k}$ is the unit normal in the direction from the centroid of cell, toward the face between cells and k , while $\vec{c}_{i,k}$ is the vector from the cell centroid to the face centroid. Additionally, T_{ik} is face transmissibility, while $T_{i,k}$ is the contribution of a cell to the face transmissibility. This transmissibility ($T_{i,k}$) is referred to as a half-transmissibility because a pair of cells contributes to the transmissibility of each face in the two-point flux approximation formulation. Note that the temporal and spatial discretizations of the continuous partial differential equations lead to a mass imbalance, which is represented by the residual (R) in Eqs. A-9 through A-12. The Newton-Raphson method involves applying the Taylor expansion to the residual at the current timestep and current Newtonian iteration to obtain:

$$\frac{\partial R^{k+1}}{\partial X} \Delta X = -R^{k+1}(X), \quad (\text{A-16})$$

where X denotes the primary variables. The matrix that contains the partial derivatives of the residuals with respect to each of these primary variables ($\frac{\partial R^{k+1}}{\partial X}$) is referred to as the Jacobian matrix. The setup of this matrix is facilitated using automatic differentiation in MATLAB Reservoir Simulation Toolbox, and more details on the solution of the system of equations for compositional flow are provided in Møyner and Tchelepi (2017). Considering that most shale/tight oil reservoirs are naturally fractured to some extent, this work will

involve simulating the proposed SDEOR method in such reservoirs with or without natural fractures. The next section explains how the discretized governing equations are modified to model natural fractures accurately and efficiently.

Appendix B—Compositional Fluid Data

Tables B-1 and B-2 provide the compositional fluid data and binary interaction constants used in the simulations that involve a simple three-component hydrocarbon fluid. **Tables B-3 and B-4** provide compositional data inputs for a representative Eagle Ford shale-oil reservoir, while provide the corresponding data for a representative Bakken shale-oil reservoir.

Components	Mole Fraction Fraction	Critical Pressure (atm)	Critical Temperature (K)	Critical Volume (L/mol)	Molar Weight (g/gMol)	Acentric Factor
C ₁	0.25	45.39	190.6	0.099	16.04	0.0114
CO ₂	0.25	72.80	304.12	0.094	44.01	0.2239
C ₁₀	0.50	20.75	617.70	0.601	142.28	0.4884

Table B-1—Compositional data for SDEOR synthetic oil fluid.

Component	C ₁	CO ₂	C ₁₀
C ₁	0	0.045	0.1050
CO ₂	0.045	0	0.1150
C ₁₀	0.1050	0.1150	0

Table B-2—Binary interaction coefficients for SDEOR synthetic oil fluid.

Components	Mole Fraction Fraction	Critical Pressure (atm)	Critical Temperature (K)	Critical Volume (L/mol)	Molar Weight (g/gMol)	Acentric Factor	Parachor Coefficient
CO ₂	0.01183	72.80	304.20	0.0940	44.01	0.225	78.01
N ₂	0.00161	33.50	126.20	0.0895	28.01	0.040	41.0
C ₁	0.11541	45.40	190.6	0.0990	16.04	0.008	77.0
C ₂ -C ₅	0.26438	36.5	274.74	0.2293	52.02	0.1723	171.07
C ₆ -C ₁₀	0.38089	25.08	438.68	0.3943	103.01	0.2839	297.42
C11+	0.22588	17.55	740.29	0.8870	267.15	0.6716	661.45

Table B-3—Compositional data for Eagle Ford shale formation, culled from Yu et al. (2019).

Component	CO ₂	N ₂	C ₁	C ₂ -C ₅	C ₆ -C ₁₀	C11+
CO ₂	0	0.02	0.1030	0.1299	0.15	0.15
N ₂	0.02	0	0.031	0.082	0.12	0.12
C ₁	0.1030	0.031	0	0.0174	0.0462	0.111
C ₂ -C ₅	0.1299	0.082	0.0174	0	0.0073	0.0444
C ₆ -C ₁₀	0.15	0.12	0.0462	0.0073	0	0.0162
C11+	0.15	0.12	0.111	0.0444	0.0162	0

Table B-4—Binary interaction coefficients for Eagle Ford shale formation, culled from Yu et al. (2019).

Components	Mole Fraction Fraction	Critical Pressure (atm)	Critical Temperature (K)	Critical Volume (L/mol)	Molar Weight (g/gMol)	RF decreases Factor	Parachor Coefficient
CO ₂	0.0002	72.80	304.20	0.0940	44.01	0.225	78.0
N ₂	0.0004	33.50	126.20	0.0895	28.01	0.040	41.0

Table B-5—Compositional data for Bakken light oil shale formation, culled from Yu et al. (2015).

Components	Mole Fraction Fraction	Critical Pressure (atm)	Critical Temperature (K)	Critical Volume (L/mol)	Molar Weight (g/gMol)	RF decreases Factor	Parachor Coefficient
C ₁	0.25	45.40	190.6	0.0990	16.04	0.008	77
C ₂ -C ₄	0.22	42.54	363.30	0.1970	42.82	0.143	145.2
C ₅ -C ₇	0.20	33.76	511.56	0.3338	83.74	0.247	250
C ₈ -C ₉	0.13	30.91	579.34	0.4062	105.91	0.286	0.099
C10+	0.1994	21.58	788.74	0.9208	200.00	0.686	0.099

Table B-5 (continued)—Compositional data for Bakken light oil shale formation, culled from Yu et al. (2015).

Component	CO ₂	N ₂	C ₁	C ₂ -C ₄	C ₅ -C ₇	C ₈ -C ₉	C10+
CO ₂	0	0.02	0.1030	0.1327	0.1413	0.15	0.15
N ₂	0.02	0	0.013	0.0784	0.1113	0.12	0.12
C ₁	0.1030	0.013	0	0.0078	0.0242	0.0324	0.0779
C ₂ -C ₄	0.1327	0.0784	0.0078	0	0.0046	0.0087	0.0384
C ₅ -C ₇	0.1413	0.1113	0.0242	0.0046	0	0.0006	0.0169
C ₈ -C ₉	0.15	0.12	0.0324	0.0087	0.0006	0	0.0111
C10+	0.15	0.12	0.0779	0.0384	0.0169	0.0111	0

Table B-6—Binary interaction coefficients for Bakken light oil shale formation, culled from Yu et al. (2015).